Journal of Geochemical Exploration 265 (2024) 107556

Contents lists available at ScienceDirect

Journal of Geochemical Exploration

journal homepage: www.elsevier.com/locate/gexplo

Ore mineralization in the Mofete and San Vito geothermal fields, Campi Flegrei volcanic complex, Naples, Italy

Harvey E. Belkin[a,*], Ryan J. McAleer[b], Benedetto De Vivo[c,d]

[a] *U.S. Geological Survey (Ret.), Geology, Energy, & Minerals Science Center, 12201 Sunrise Valley Dr., Reston, VA 20192, USA*
[b] *U.S. Geological Survey, Florence Bascom Geoscience Center, 12201 Sunrise Valley Dr., Reston, VA 20192, USA*
[c] *Pegaso Online University, Piazza Trieste e Trento 48, 80132 Naples, Italy*
[d] *Department of Geosciences, Virginia Tech, Blacksburg, VA 24061, USA*

ARTICLE INFO

Keywords:
Campi Flegrei
Mofete
San Vito
Geothermal
Ore mineralization

ABSTRACT

The Mofete and San Vito geothermal fields, located west of Naples, Italy, are part of the Campi Flegrei volcanic complex. In the 1970s, exploratory wells were drilled to a depth of ~3000 m in an attempt to locate high-enthalpy fluids for potential power production. Drill core samples from Mofete wells (MF1, MF2, and MF5) and from San Vito wells (SV1 and SV3) contain authigenic ore mineralization. Pyrite, pyrrhotite, and galena are abundant. Less common are chalcopyrite, sphalerite, arsenopyrite, and scheelite; rare are millerite, violarite, native bismuth, tellurobismuthite, cassiterite, molybdenite, and acanthite. Mineral chemistry was determined by electron microprobe wavelength dispersive spectroscopy aided by a scanning electron microscope equipped with energy-dispersive spectroscopy. The mineral assemblage suggests a low sulfidation environment and the absence of pyrrhotite in the MF1 well and upper part of the SV1 well indicates variable sulfur activity. Both molybdenite and scheelite were identified in samples SV1–2860 and SV3–2353 and scheelite in the SV3 well is zoned with variable Mo^{6+} content; low Mo^{6+} zones show blue cathodoluminescence, whereas, zones with high Mo^{6+} content are yellow to brown. Zoned scheelite and the occurrence of both Mo-bearing minerals attest to the variability of fO_2 and fS_2 in the geothermal fluid.

1. Introduction

Magmatic-related hydrothermal systems form where heat drives extensive fluid flow, and these systems often have a component of fluid directly exsolved from the cooling magma (Mahon and McDowell, 1977; Hedenquist and Lowenstern, 1994). Ore deposits form in these systems and have supplied significant metals to society through millennia. Detailed analysis of ancient and active magma-generated geothermal systems can provide an excellent analogue for near surface ore-mineralization environments (e.g., White, 1981; Sander and Mitchell, 1988; Bogie et al., 2000). Although young geothermal systems rarely contain economic ore deposits, they are especially important to investigate as active fluid transportation, depositional processes, and authigenic mineral deposition can be studied from either surface manifestations or by drilling. Although we use the term “ore mineral”, we do not suggest that we have found or that an ore deposit exists or is forming in the Campi Flegrei area.

The Campi Flegrei volcanic complex, located west of Naples in southern Italy (Fig. 1), has extensive surface manifestations, hot springs, and fumaroles to the extent that the early Greek settlers named the area Phlegrean Fields, translated as ‘burning fields’. Lake Avernus, which occupies a crater in Campi Flegrei, was thought to be the entrance to Hades as portrayed by Virgil in the Aeneid and the Romans have used the extensive thermal-mineral hot springs since Imperial time (Giacomelli and Scandone, 2012). Although the extensive exploration drilling by a joint venture between the Italian Geodynamic Project and the Italian national electric and petroleum utilities (Rosi and Sbrana, 1987; Carlino et al., 2012) for high enthalpy fluids did not locate any geothermal fields with sufficient flow to be useful to generate electricity, there have been recent proposals to use the geothermal fields for a variety of other uses (e.g., Barbato et al., 2018). Recently, there have been studies of the Agnano geothermal field in the Campi Flegrei area to investigate the potential for low–middle enthalpy resource exploitation (Iorio et al., 2024). The Italian Geodynamic Project exploration program produced much drill core and geochemical and geophysical knowledge to a depth of about 3 km (Rosi and Sbrana, 1987; De Vivo et al., 1989).

---

* Corresponding author.
E-mail addresses: harveybelkin@gmail.com (H.E. Belkin), rmcaleer@usgs.gov (R.J. McAleer), devivob@libero.it (B. De Vivo).

https://doi.org/10.1016/j.gexplo.2024.107556
Received 2 March 2024; Received in revised form 30 June 2024; Accepted 25 July 2024

Early detailed studies of this drill core investigated fluid inclusions, mineralogy, and other geochemical and geophysical parameters (e.g., Chelini and Sbrana,1987; De Vivo et al., 1989; Altaner et al., 1991; Zamora et al., 1994; Caprarelli et al., 1997; Belkin and De Vivo, 2004). More recently, some of the Mofete and San Vito core has been studied: (1) to examine water-rock reactions as an aid to geochemical modeling (Piochi et al., 2021), (2) to examine the subsurface structure (Piochi et al., 2014), (3) to study the secondary hydrothermal mineral assemblage in relation to rock physics and the state of the volcanic system (Mormone et al., 2011), and (4) to document the compositional variation and zoning of epidote supergroup minerals (Belkin and De Vivo, 2023). These four studies identified only two sulfides, pyrite and pyrrhotite, and no compositional data were given.

During detailed investigations of the Campi Flegrei drill core for a previous study of fluid inclusions (De Vivo et al., 1989), we observed the occurrence of a diverse group of metal sulfides, tungstate, telluride, oxide, and native element phases. Their texture indicated that these phases were authigenic and were deposited by geothermal fluids. Our goal in this report is to document the distribution, petrography, and mineral chemistry of these authigenic ore minerals.

2. Geologic setting

The Campi Flegrei caldera complex is part of an active volcanic region developed on the subsiding western margin of the Apennine Chain (Fig. 1). Although the region has been active intermittently during the last 600 ka (Belkin et al., 2016), a major event occurred in 39 ka (De Vivo et al., 2001) with the very large eruption (310 km^3) of the Campanian Ignimbrite (Rolandi et al., 2003). Early studies (e.g., Barberi et al., 1978; Rosi et al., 1983) of the Campanian Ignimbrite assumed that the large Campi Flegrei caldera was the result of this eruption, but recent data suggest that the caldera was formed by the younger Neapolitan Yellow Tuff (NYT) eruption (Rolandi et al., 2020a), and that the Campanian Ignimbrite erupted from fissures north of the NYT caldera (Rolandi et al., 2020b). Subsequent to NYT event, the Campi Flegrei region has had much volcanic activity ending with the Monte Nuovo eruption of 1538 CE (Di Vito et al., 1987; Piochi et al., 2005). The chemistry of all the products is Si-undersaturated, low in MgO, but rich in alkalis. Trachyte and alkali-trachyte are predominant volumetrically with much lesser amounts of trachybasalt, latite, and peralkaline-phonolitic-trachyte (Rosi and Sbrana, 1987). The chemistry of the rock penetrated by the Mofete and San Vito wells is generally similar from top to bottom although some wells end in hydrothermally metamorphosed marine siltstones and sandstones (Rosi and Sbrana, 1987).

The Campi Flegrei hydrothermal system is still active with major fumarolic activity at Solfatara and Pisciarelli (Fig. 1; Fedele et al., 2017; Bagnato et al., 2020; Isaia et al., 2021; Marini et al., 2022) as well as the numerous hot springs (e.g., Valentino and Stanzione, 2003) and other

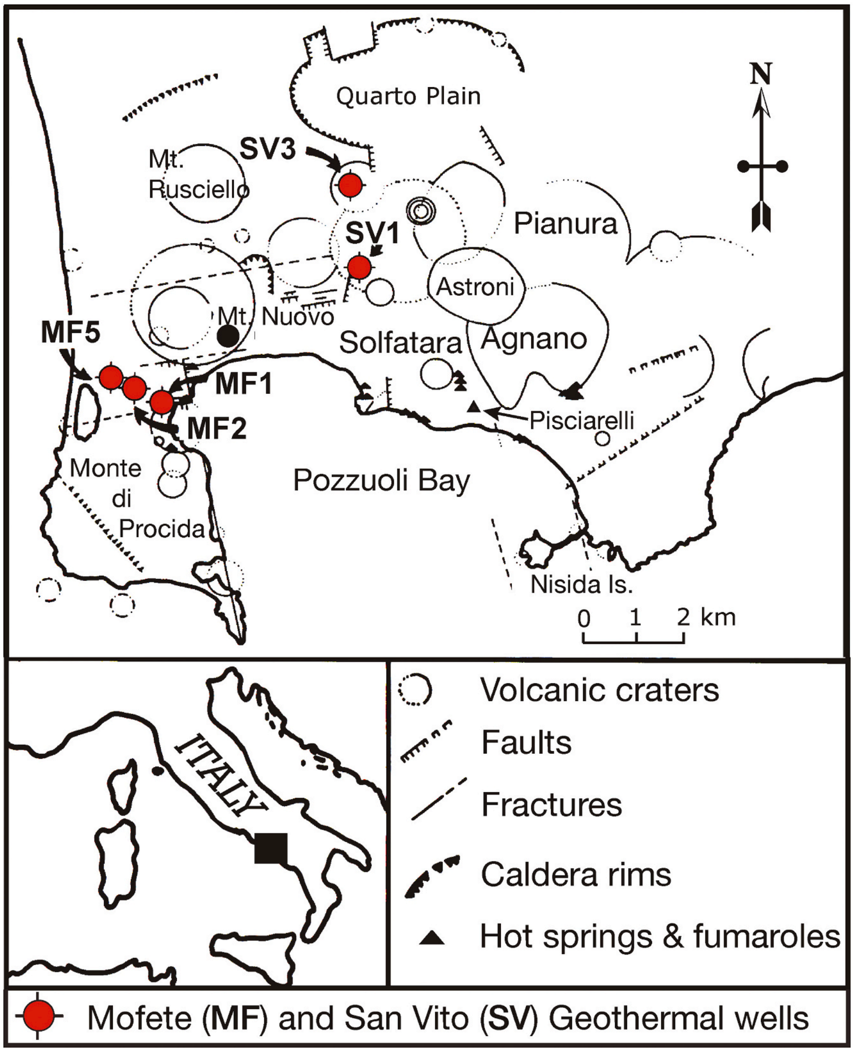

Fig. 1. Schematic location map adapted from De Vivo et al. (1989) showing various geologic features in the Campi Flegrei volcanic complex, and the positions of the five geothermal wells MF1 (40.824N, 14.069E), MF2 (40.826N, 14.065E), MF5 (40.831N, 14.060E), SV1 (40.849N, 14.121E), and SV3 (40.864N, 14.121E).

hydrothermal manifestations in the region (Chiodini et al., 2022). Bradyseismic events are also attributed to hydrothermal fluid movement at depth (e.g., Gaeta et al., 1998; De Vivo and Lima, 2006; Bodnar et al., 2007; Lima et al., 2009, 2021; Troise et al., 2019).

3. Samples studied

We obtained the Mofete (MF) and San Vito (SV) samples in 1985 from the joint venture drilling program between the Italian Geodynamic Project and the Italian national utilities, Agip and Enel (both now privatized) (Rosi and Sbrana, 1987). The initial selection of core was designed for a fluid inclusion study (De Vivo et al., 1989), which emphasized the deeper, hotter parts of the geothermal system, hence our study does not cover the shallow part of the geothermal system. The Campi Flegrei geothermal system is liquid-dominated and exhibits evidence of boiling in the upper portions, and fluid reservoirs of different salinity (De Vivo et al., 1989; Caprarelli et al., 1997). The lithologic and mineralogic details of the studied samples are described in De Vivo et al. (1989). Generalized stratigraphic columns are given in Piochi et al. (2014; MF5 and SV1) and Mormone et al. (2011; MF2 and SV1) and cross sections of both the San Vito and Mofete areas are given in Belkin and De Vivo (2023; Fig. 2). Table 1 lists the samples containing the ore minerals, which come from the Mofete 1 (MF1), Mofete 2 (MF2), Mofete 5 (MF5), San Vito 1 (SV1), and San Vito 3 (SV3) exploratory geothermal wells (Fig. 1). Although some of the cores were sampled from an interval of several meters, the sample numbers are based on the top of the

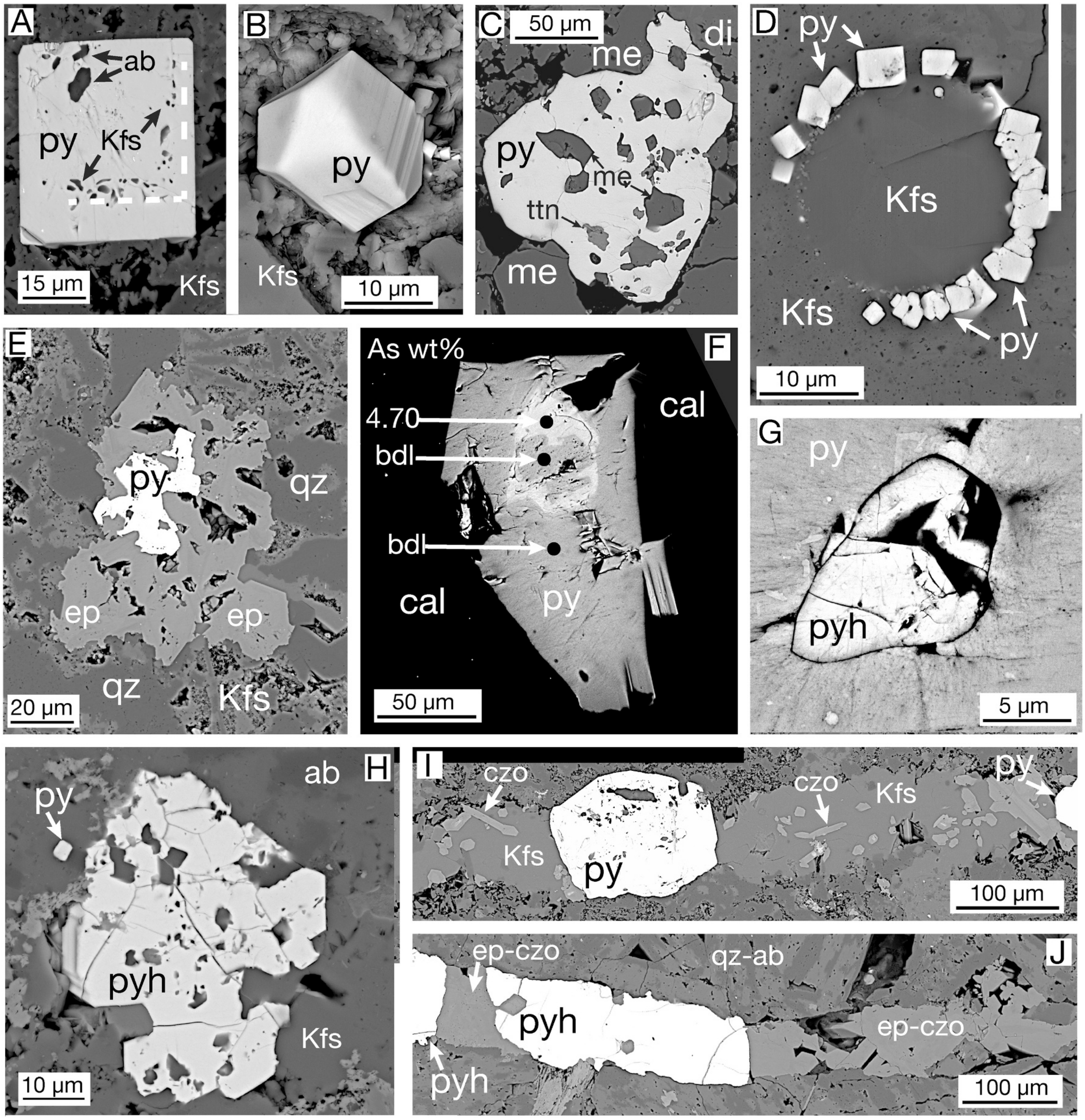

Fig. 2. All BSE images: A) Pyrite (py) cube in K-feldspar (Kfs) showing two types of inclusions: 1- large irregular-shaped solid albite (ab) inclusions and 2 - K-feldspar inclusions trapped along growth zones marked by the dashed line, sample MF1-1398; B) euhedral pyrite (py) with pyritohedron form in K-feldspar, quartz, and clay, sample MF1-928; C) anhedral pyrite (py) containing meionite (me) and titanite (ttn) inclusions with diopside (di) and meionite, sample SV3-2353; D) ring of pyrite (py) cubes around a former vesicle now filled with K-feldspar (Kfs) in K-feldspar, sample SV1-2860; E) a pyrite (py) core of an epidote (ep) mass in quartz (qz) and K-feldspar (Kfs), sample MF1-1495, modified from Belkin and De Vivo (2023); F) subhedral pyrite showing three stages of formation with different As (wt%) contents, from 4.70 wt% to bdl (below detection limit <0.3 wt%) in calcite (cal), sample MF1-928; G) residual pyrrhotite (pyh) included in pyrite (py), sample SV3-2353; H) anhedral pyrrhotite (pyh) containing many K-feldspar and albite inclusions in albite (ab) and K-feldspar (Kfs); small euhedral pyrite (py) cube is indicated by arrow, sample MF2-1715; I) portion of a 10 mm-long vein composed of pyrite (py), K-feldspar (Kfs), and small crystals of clinozoisite (czo), sample MF1-1597; J) portion of a 15 mm-long vein composed of pyrrhotite (pyh) and zoned epidote-clinozoisite (ep-czo) in a quartz-albite (qz-ab) matrix, sample MF2-1824.

Table 1
Distribution of mineralization in Mofete and San Vito core samples.

Sample[a]	py	pyh	gn	ccp	sp	apy	aca	sch	mol	cas	Ni	Bi	T °C[b]	Alteration zone
MF1-928	X		X	X		X							255	C
MF1-1150	X		X	X	X	X		X					275	C
MF1-1299	X		X										295	C
MF1-1398	X		X			X		X					308	C
MF1-1495	X		X			X		X		X			320	C
MF1-1597	X		X	X				X					347	C
MF2-1582	X		X				X						315	C
MF2-1715	X	X			X	X							325	C
MF2-1824		X				X	X						335	C
MF5-2605		X			X	X		X			X		350	D
MF5-2610	X	X	X									X	350	D
SV1-1715	X		X										285	C
SV1-1720	X		X										285	C
SV1-2125	X		X	X	X			X					300	C
SV1-2510	X												335	C
SV1-2676	X	X	X										350	D
SV1-2860	X	X	X				X	X	X	X		X	390	D
SV3-2105	X			X			X	X			X		320	D
SV3-2353	X	X	X	X				X	X		X		330	D
SV3-2359	X	X	X	X	X		X	X		X			330	D

py = pyrite, pyh = pyrrhotite, gn = galena, ccp = chalcopyrite, sp. = sphalerite.
apy = arsenopyrite, aca = acanthite, sch = scheelite, mol = molybdenite.
cas = cassiterite, Ni = nickel phases, Bi = bismuth phases.
C = calcium-aluminumsilicate zone, D = thermometamorphic zone.

[a] Well and depth (m) to the top of the sampling interval.

[b] Measured well temperature after stabilization (De Vivo et al., 1989).

interval (Table 1). On the basis of detailed petrography and X-ray diffraction analysis, Chelini and Sbrana (1987) defined four descending hydrothermal zones with different characteristic mineralogy: argillic, chlorite-illite, calcium-aluminum silicate, and thermometamorphic. The calcium-aluminum silicate zone is characterized by abundant epidote and quartz, feldspars, various sulfides, and layered silicates. The temperature at the top of this zone as defined by Chelini and Sbrana (1987) is about 250 °C in the Mofete area, but was less well defined in San Vito area at between 220° to 270 °C. The bottom of this zone was assessed by Chelini and Sbrana (1987) to be at 325 °C in the Mofete area, whereas in San Vito 1 it corresponds to the current 360 °C isotherm, and in San Vito 3 it corresponds to the current 270 °C isotherm. This lower temperature in San Vito 3 reflects the complexity of recent faulting and De Vivo et al. (1989) suggest hotter temperatures were present during mineral formation. The thermometamorphic zone is characterized by two subzones, amphibole-biotite and diopside, where both show nearly complete recrystallization and/or replacement of the host rock (Chelini and Sbrana, 1987). All the studied samples come from the calcium-aluminum silicate and the thermometamorphic zones.

4. Methods

Petrographic examination and preliminary mineral identification were done on polished thin sections with a JEOL JSM-840 scanning electron microscope (SEM) using a LaB_6 electron emitter equipped with a Princeton Gamma Tech Si(Li) energy-dispersive X-ray spectrometer (EDS) and a Hitachi SU5000 Schottky thermally assisted field emission SEM equipped with an Oxford Ultima 100 mm^2 EDS silicon drift detector with Oxford AZtec software. The samples were examined optically and by SEM back-scattered electron (BSE) imaging to define points for analysis. Quantitative electron microprobe analyses (EPMA) of major and minor elements were obtained in Reston, VA, with a JEOL JXA-8900R five spectrometer, fully automated electron microprobe using wavelength-dispersive X-ray spectrometry (WDS). Analyses for all minerals described below were made at 20 kV accelerating voltage and 30 nA probe current, and counting times of 20 to 120 s, using a 1 or 2 μm diameter probe spot. Standard reference materials were appropriate synthetic or natural reference materials available in the U.S. Geological Survey Reston Microbeam Laboratory (Huebner and Woodruff, 1985). The analyses were corrected for electron beam/matrix effects, and instrumental drift and deadtime using a Phi-Rho-Z (CITZAF; Armstrong, 1995) algorithm as supplied with the JEOL JXA-8900R electron microprobe. Relative accuracy of the analyses, based upon comparison between measured and published compositions of standard reference materials, is ~1–2 % for concentrations >1 wt% and ~ 5–10 % for concentrations <1 wt%. Detection limits (wt%) at the three-sigma level were Al (0.02), Ag (0.05), As (0.03), Au (0.10), Bi (0.10), Ca (0.02), Cd (0.03), Co (0.02), Cu (0.02), Fe (0.02), Hg (0.30), Mg (0.02), Mn (0.02), Mo (0.04), Na (0.02), Ni (0.02), Pb (0.15), S (0.02), Sb (0.02), Se (0.02), Si (0.02), Sr (0.04), Te (0.10), W (0.05), and Zn (0.03).

Some minerals were too small, in cracks or vugs, or poorly polished and hence were not amenable for EPMA experiments, but were easily identified with EDS spectra. To obtain compositions for some of these phases we used the Oxford AZtec EDS beam measurement system with the extended set of factory element standardization. Operating conditions were 20 kV, 40 spot position (~1.7 nA probe current), 10 mm working distance, and 200 s live counting time. Cathodoluminescence (CL) images were collected with a Delmic SPARC cathodoluminescence detector attached to a Hitachi SU5000 Schottky thermally assisted field emission SEM. The color CL images were obtained using a filter wheel and serial collection of blue (<505 nm), green (505–575 nm), and red (>605 nm) channels with a photomultiplier tube detector.

The full data set for pyrite, pyrrhotite, chalcopyrite, sphalerite, galena, arsenopyrite, Ni-sulfides, and scheelite can be found in Belkin et al. (2023) and in the supplementary tables (S1–S8).

5. Results - petrography and mineral chemistry

Mineralization in the Mofete and San Vito fields comprises sulfide, native element, telluride, oxide, and tungstate phases (Figs. 2A–J, 3A–I, 4A–H, 5A–G). Table 1 gives the distribution of the mineralization identified in the Mofete and San Vito drill core samples.

5.1. Pyrite

Pyrite (FeS_2) was the most abundant sulfide found in terms of volume

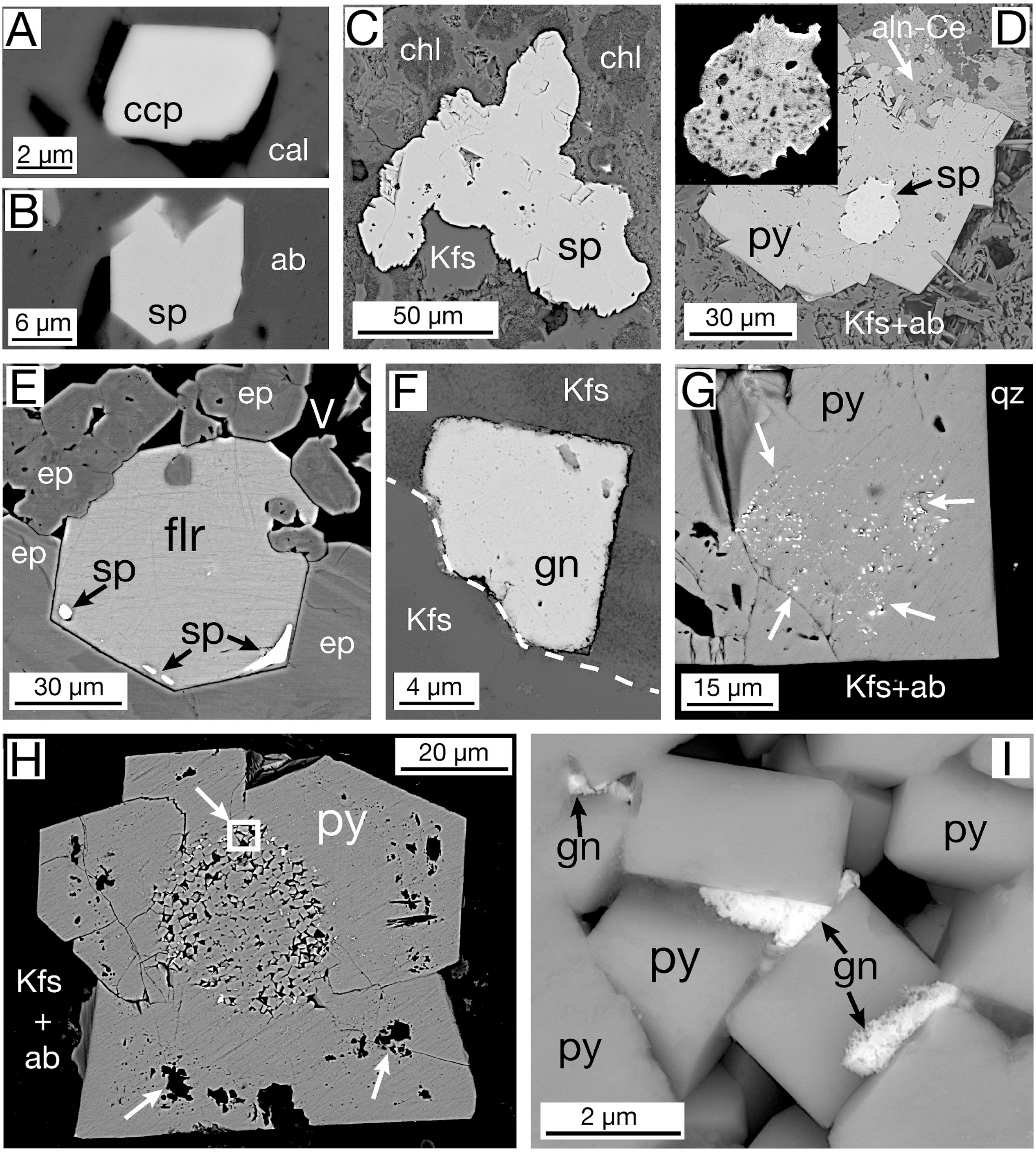

Fig. 3. BSE images: A) Euhedral chalcopyrite (ccp) in an open space in calcite (cal), sample MF1-928; B) euhedral sphalerite (sp) in an open space in albite (ab), sample MF2-1715. C) A large anhedral mass of sphalerite (sp) in a mixture of chlorite (chl) and K-feldspar (Kfs), sample SV1-2125; D) a sphalerite (sp) inclusion in pyrite (py). The enlarged high-contrast inset shows the pattern of chalcopyrite disease in the inclusion. K-feldspar (Kfs), albite (ab), and allanite-(Ce) (aln-Ce) surround the pyrite, sample MF1-1150; E) a euhedral fluorite (flr) crystal that has inclusions of sphalerite (sp) close to three corners. Hosted by epidote (ep) on the edge of a vug (V), sample SV3-2359; F) a euhedral galena (gn) crystal that grew on the edge of K-feldspar (lower Kfs below dashed line), then covered by later fine-grained K-feldspar, sample SV1-2125; G) mass of hundreds of minute galena inclusions (arrows) in the corner of a pyrite (py) cube in quartz (qz), K-feldspar (Kfs), and albite (ab), sample MF1-1495. H) A large multi-crystal of pyrite (py) that grew around a mass of smaller pyrite crystals. Upper arrow shows area enlarged in I. Lower arrows indicate albite and K-feldspar inclusions that occur near the terminations of all the pyrite crystals. Surrounded by K-feldspar (Kfs) and albite (ab), sample MF1-1495; I) enlarged area from H, showing late-stage masses of sub-micrometer galena (gn) crystals growing among euhedral pyrite (py).

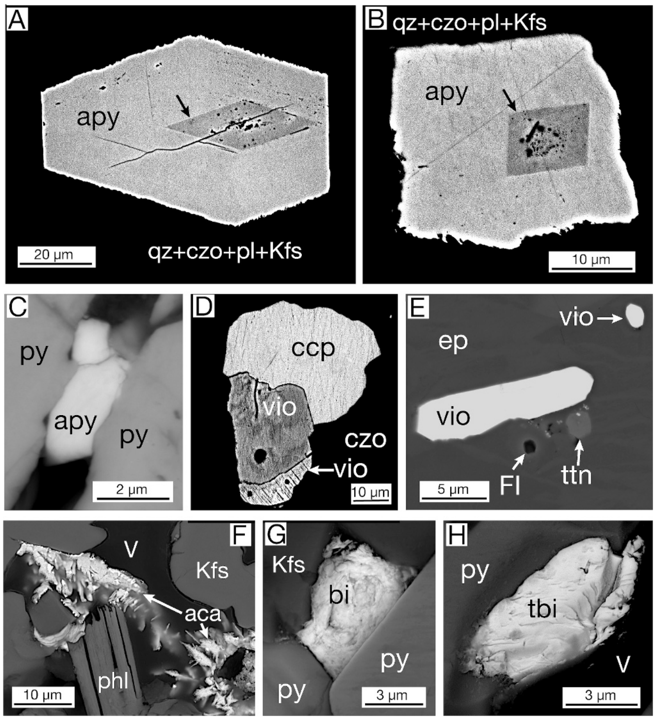

Fig. 4. BSE images: A) Euhedral arsenopyrite (apy) with a euhedral core (arrow) of Co-poor arsenopyrite surrounded by a Co-rich rim, sample MF5-2605; B) subhedral arsenopyrite (apy) with a euhedral core (arrow) of Co-poor arsenopyrite surrounded by a Co-rich rim, sample MF5-2605. Both A and B occur in a mix of quartz (qz), clinozoisite (czo), plagioclase (pl) and K-feldspar, and both the inner zones have inclusions (dark spots) of quartz, K-feldspar, and clinozoisite; C) arsenopyrite (apy) in the space between two pyrites (py), sample MF1-928; D) chalcopyrite (ccp) later than violarite (vio) with a more Ni-rich violarite (lower vio), in epidote (ep), sample SV3-2353; E) two euhedral violarite (vio) grains in epidote with titanite (ttn) and a fluid inclusion (FI) intersected by sample preparation, sample SV3-2353; F) A mass of arborescent acanthite (aca) around phlogopite (phl), K-feldspar (Kfs), and a vug (V) now filled with epoxy, sample MF2-1854; G) native bismuth (bi) in between pyrite (py) and K-feldspar (Kfs), sample MF5-2610; H) tellurobismuthite (tbi) between the open space (V) of two pyrite (py) grains with the lower right pyrite grain not shown, sample MF5-2610.

in the drill cores. We identified it in all samples except MF2–1824 and MF5–2605 (Table 1; see Section 6.1 for discussion). It occurred in various crystal habits including cubes (Fig. 2A), pyritohedrons (Fig. 2B), and amoeboid-shaped subhedral to anhedral masses (Fig. 2C). The subhedral and anhedral shapes ranged in size from ~20 µm to ~3 mm, whereas the euhedral crystals, the most abundant, ranged in size from ~1 µm to 0.8 mm; pyritohedrons were rare and were all <20 µm. In a few cases we observed pyrites outlining (Fig. 2D) or filling (Fig. 3H) what may have been vesicles or pores. Solid inclusions are very common in pyrite, some follow growth zones (Fig. 2A), whereas most appear to be randomly trapped (Fig. 2C). Anhedral pyrite masses were early in the sequence of authigenic mineral precipitation and are observed in the cores of zoned epidote group masses (Fig. 2E; see Belkin and De Vivo, 2023). Pyrite is also common in later cross-cutting silicate (Fig. 2I) and calcite veins.

Pyrite (FeS_2) commonly contains minor elements substituting for either S or Fe. Copper, Zn, Mn, Pb, and Sb were all <0.2 wt%; only As, Co, and Ni were > 1.0 wt%, but only in some grains. In the Mofete samples, the element ranges are the following in wt%: As dl (detection limit)–4.89, Cu dl–0.09, Zn dl–0.12, Co dl–1.67, Mn dl–0.07, Pb dl–0.16, Sb dl–0.03, and Ni dl–0.39. In the San Vito samples, the element ranges are the following in wt%: As dl–0.03, Cu dl–0.07, Zn dl–0.03, Co dl–0.99, Mn dl–0.05, Ni dl–1.43, Pb and Sb - not detected. For both Mofete and San Vito pyrite, Au and Se were not detected.

Most pyrite in the Mofete and San Vito samples is unzoned. When we did observe zoning in BSE images, we were interested in what elements were involved and preferentially analyzed those grains; therefore, the number of zoned pyrites in Table 2 is not representative of the frequency of zoning. Mofete samples were zoned in As, whereas, San Vito samples were zoned in Ni. One pyrite grain in sample MF1–928 had a ring shape exceptionally enriched in As (4.70 wt%), whereas, the core and rim were below detection for As (Fig. 2F). For the Mofete samples, about half had high As cores with low As rims and about half had the opposite, high As rims, with low As cores. In the two zoned grains in the San Vito samples, the cores had higher Ni than the rims. Table 2 gives representative compositions of pyrite.

5.2. *Pyrrhotite*

Pyrrhotite (Fe_7S_8) was a common Fe sulfide mineral in all the wells, except MF1 and the upper part of SV1 (see Section 6.2 discussion below). Grains were typically amoeboid anhedral or subhedral (Fig. 2H); euhedral grains were uncommon and small. Where we could observe the textural relationship between pyrrhotite and pyrite, pyrrhotite formed earlier, and sometimes as an inclusion in pyrite (Fig. 2G), or the pyrite was in the later-stage minerals surrounding pyrrhotite (Fig. 2H). Pyrrhotite ranged in size from ~3 µm to ~0.5 mm and was unzoned. Pyrrhotite commonly contains minor elements substituting for Fe and S. We detected As, Cu, Ni, Co, and Mn, but all were very low (<0.15 wt%), except for an inclusion in pyrite that had Cu 0.27 and Ni 0.55 wt% (Table 3, Fig. 2G). Table 2 gives representative compositions of pyrrhotite.

5.3. *Chalcopyrite*

Chalcopyrite ($CuFeS_2$) was an uncommon sulfide in all the wells except SV3 (Table 1). In many cases the grains were small (Fig. 3A), in cracks in pyrite, poorly polished, and not amenable for EPMA, although were readily identified by EDS. Minor elements in chalcopyrite include Ni, Zn, and Co and were all below 0.5 wt%; Pb and Se were below detection (Table 4). We identified chalcopyrite disease (Barton Jr. and Bethke, 1987), in sphalerite, but could not get an acceptable analysis (see Section 5.4).

5.4. *Sphalerite*

Sphalerite (ZnS) was an uncommon sulfide in all the wells (Table 1), but where it did occur, it was relatively abundant. Small crystals were identified as inclusions in calcite veins (Fig. 3A) as well as in pyrite. Irregular shaped large masses, unzoned, trapped small silicate inclusions (Fig. 3B). We also observed anhedral sphalerite with chalcopyrite disease (Barton Jr. and Bethke, 1987) either as inclusions in pyrite (Fig. 3D) or isolated. The blebs of chalcopyrite are irregular in shape and range in size from 1 to 3 µm. We observed chalcopyrite disease only in sample MF1–1150 in anhedral grains with a rough outline. In a few cases, sphalerite was also associated with fluorite (Fig. 3E).

For those sphalerites with disease, EMPA data were difficult to obtain without electron beam excitation of the chalcopyrite blebs; EMPA Cu values ≥2 wt% were assumed have included chalcopyrite except for a 3 µm sphalerite inclusion having 2.99 wt% Cu found in pyrite (Table 5). Arsenic and Se were detected in trace amounts at or just above their respective detection limits. Copper varies from 1.79 wt% to dl and Mn was relatively uniform and ranged from 0.25 to 0.12 wt%. Iron varies from 1.78 to 11.85 wt% and FeS mole% ranged from 3.4 to 20.7. Although Cd is a common element in substitution for Zn, we observed only four sphalerite crystals with detectable Cd, which varied from 0.07 to 0.18 wt%. Table 5 gives representative compositions of sphalerite.

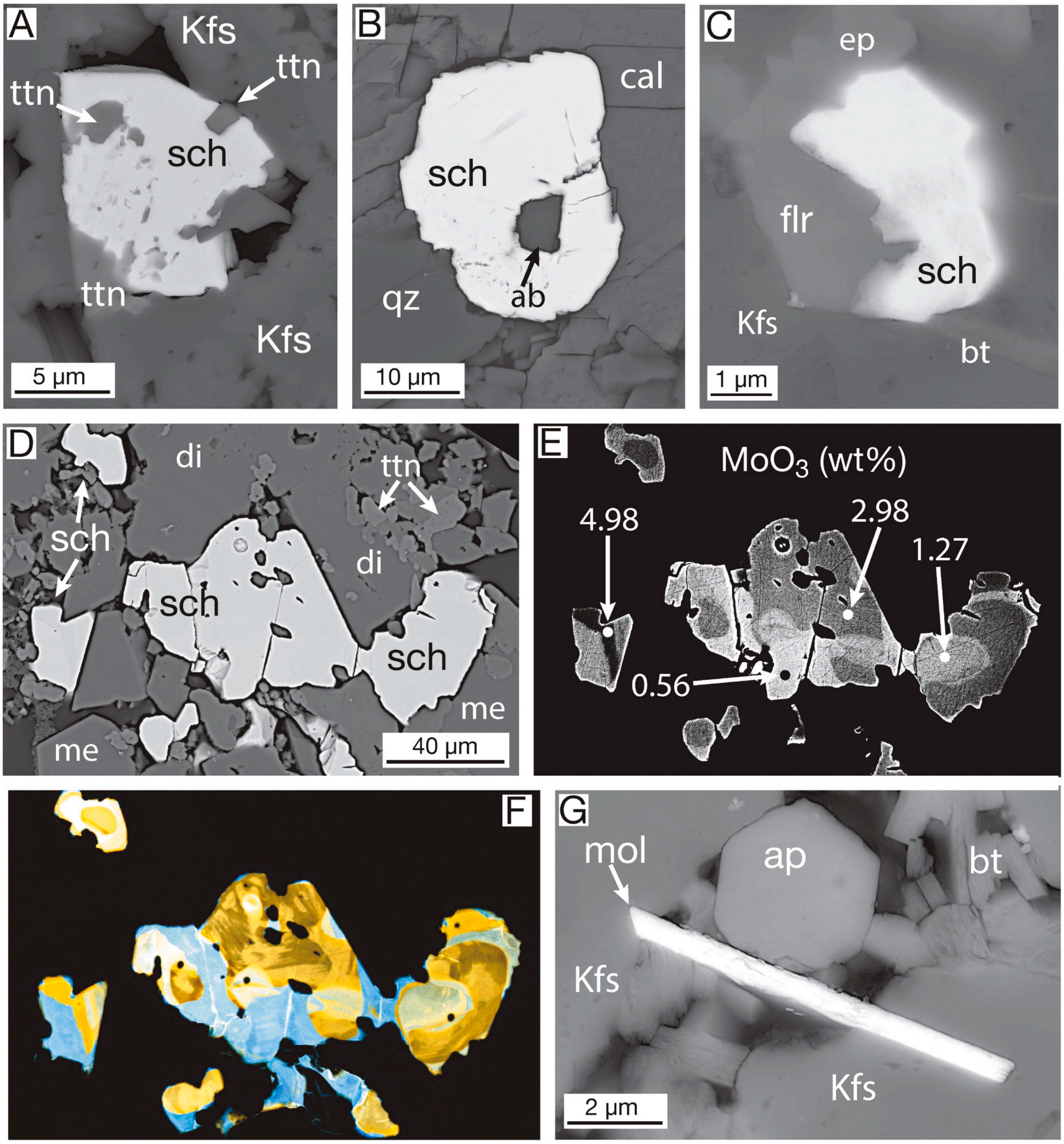

Fig. 5. BSE images except where noted: A) Unzoned scheelite (sch) in vug (dark area) in K-feldspar (Kfs) with titanite inclusions (ttn), sample MF1-1150; B) unzoned scheelite in quartz (qz) and calcite (cal) with an albite (ab) inclusion, sample MF1-1398; C) unzoned scheelite (sch) with fluorite (flr) surrounded by K-feldspar (Kfs), epidote (ep), and biotite (bt), sample SV1-2125; D) zoned scheelite (sch; white grains in BSE)) filling open spaces created by diopside (di), meionite (me), and minor titanite (ttn), sample SV3-2353; E) same area as D, but with greatly enhanced BSE contrast to show zoning in scheelite. Analyzed spots are marked with the weight percent of MoO_3 and are given in Table 9; F) same area as D showing only RGB cathodoluminescence; G) typical blade of molybdenite (mol) in a vug with apatite (ap), biotite (bt), and K-feldspar (Kfs), sample SV1-2860.

5.5. Galena

Galena (PbS) is mostly a late-stage mineral in the wells. Euhedral or subhedral crystals (Fig. 3F) are uncommon and are small relative to the iron sulfides. Most galena occurs as inclusions either trapped by the growing crystal (Fig. 3G), precipitated in pores of crystal aggregates (Fig. 3H, I), or in cracks between pyrite or silicates; some in cracks were as large as 45 μm. We only found galena inclusions in pyrite, not in pyrrhotite. Galena maybe the most numerous sulfide in the wells due to its occurrence as multitudes of micrometer-size inclusions.

Galena is not zoned and contains minor amounts of trace elements. Copper, Se, Ag, and Cd were detected, but in amounts usually <0.2 wt%. A few high values of Fe, we attribute to the analyzed galena as an inclusion or adjacent to pyrite. Table 6 gives representative compositions.

5.6. Arsenopyrite

Arsenopyrite (FeAsS) was observed only in the Mofete wells (see Section 6.2 discussion), but only in MF5–2605 was it abundant (Table 1). In MF5–2605, euhedral to subhedral crystals (Fig. 4A, B) are widely distributed in a matrix of quartz, clinozoisite, and alkali and plagioclase feldspar. High contrast BSE shows zoning in many crystals (Fig. 4A, B) and this is reflected in the minor element abundance. We suspect that all arsenopyrite in thin section MF5–2605 is zoned, but the zoning may not be at the surface due to the grain orientation during thin section preparation. We also identified arsenopyrite as small inclusions between pyrite grains (Fig. 4C) or in the pyrite. Those arsenopyrite grains in cracks or inclusions, except one, were not amenable to EPMA experiments, but were identified by EDS.

Table 2
Representative compositions of pyrite.

Analysis no.	Zoned		MF1-928a.11	MF1-1150.9	MF1-1495.2	Zoned		MF1-1495.2	MF2-1582.1	MF5-2610.6	SV1-2125.2	SV1-2510.13	Zoned		SV3-2353.2a
	MF1-928b.16HighZ	MF1-928b.16rim				MF1-1495.7rim	MF1-1495.7core						SV3-2353.4rim	SV3-2353.4core	
Size	200 μm	200 μm	25 μm	100 μm	100 μm	120 μm	120 μm	100 μm	5 μm	850 μm	200 μm	50 μm	60 μm	60 μm	55 μm
Comment	Subhedral	Subhedral	Euhedral	Subhedral	Euhedral	Euhedral	Euhedral	Euhedral	Euhedral	Subhedral	Subhedral	Euhedral	Anhedral	Anhedral	Subhedral
n=	1	1	1	3	1	1	2	1	1	3	2	1	1	1	1
S (wt%)	50.90	54.01	52.27	52.49	51.96	52.41	53.25	51.96	51.79	53.30	53.67	53.45	52.88	53.99	52.63
As	4.70	bdl	bdl	0.15	0.85	1.30	0.78	0.85	0.25	bdl	bdl	bdl	bdl	bdl	bdl
Cu	bdl	bdl	0.03	bdl	bdl	0.02	bdl	bdl	0.06	bdl	bdl	0.06	0.03	bdl	0.02
Zn	bdl	bdl	0.04	bdl	bdl	bdl	bdl	bdl	bdl	bdl	bdl	bdl	bdl	bdl	bdl
Co	bdl	bdl	0.06	bdl	0.26	1.67	0.23	0.26	0.19	0.04	0.14	0.12	bdl	0.04	0.99
Fe	46.22	46.33	43.87	47.43	45.50	44.39	45.80	45.50	44.67	46.58	45.57	46.03	45.79	44.95	45.27
Mn	bdl	bdl	bdl	bdl	bdl	bdl	bdl	bdl	0.04	0.02	bdl	bdl	bdl	bdl	0.04
Pb	bdl	bdl	bdl	bdl	0.09	bdl	bdl	0.09	bdl	bdl	bdl	bdl	bdl	bdl	bdl
Sb	bdl	bdl	bdl	bdl	bdl	bdl	bdl	bdl	0.03	0.02	bdl	bdl	bdl	bdl	bdl
Ni	0.05	0.03	0.11	bdl	0.03	0.39	0.03	0.03	bdl	0.07	bdl	bdl	0.52	1.43	0.03
Total	101.87	100.37	96.38	100.09	98.69	100.18	100.09	98.69	97.03	100.02	99.38	99.66	99.21	100.42	99.01
S (at.%)	64.057	66.996	67.399	65.793	66.099	65.952	66.552	66.099	66.645	66.544	67.162	66.834	66.670	67.324	66.448
As	2.532	0.000	0.000	0.079	0.462	0.697	0.416	0.462	0.139	0.000	0.000	0.000	0.000	0.000	0.000
Cu	0.000	0.000	0.020	0.000	0.000	0.014	0.003	0.000	0.038	0.000	0.000	0.041	0.017	0.000	0.015
Zn	0.000	0.000	0.025	0.000	0.000	0.000	0.000	0.000	0.002	0.000	0.000	0.000	0.000	0.000	0.000
Co	0.000	0.000	0.042	0.000	0.182	1.141	0.156	0.182	0.131	0.027	0.098	0.081	0.000	0.026	0.680
Fe	33.395	32.995	32.477	34.128	33.229	32.067	32.863	33.229	33.006	33.385	32.738	33.044	33.141	32.181	32.816
Mn	0.000	0.000	0.000	0.000	0.000	0.000	0.000	0.000	0.029	0.015	0.000	0.000	0.000	0.000	0.029
Pb	0.000	0.000	0.000	0.000	0.017	0.000	0.000	0.017	0.000	0.000	0.000	0.000	0.000	0.000	0.000
Sb	0.000	0.000	0.000	0.000	0.000	0.000	0.000	0.000	0.009	0.007	0.000	0.000	0.000	0.000	0.000
Ni	0.017	0.010	0.037	0.000	0.010	0.129	0.009	0.010	0.000	0.023	0.000	0.000	0.172	0.469	0.011

n = number of analyses averaged; bdl = below detection limit; cal = calcite; Se, Au = bdl.

Table 3
Representative compositions of pyrrhotite.

Analysis no.	MF2-1824.3	MF2-1824.7	MF2-1824.8	MF2-1824.6	MF5-2605.4	MF5-2605.13	SV1-2860.3	SV1-2860.9	SV1-2860.12	SV3-2353.13
Size	360 μm	50 μm	250 μm	125 μm	100 μm	65 μm	195 μm	105 μm	95 μm	5 μm
Comment	Anhedral	Subhedral	Subhedral	Anhedral in vein	Subhedral	Anhedral	Subhedral	Subhedral	Subhedral	Incl in py
n=	1	1	1	1	3	1	3	3	3	1
S (wt%)	38.29	38.57	38.59	38.34	38.16	38.99	39.16	39.25	39.35	38.29
As	0.03	bdl	bdl	bdl	bdl	bdl	bdl	bdl	bdl	bdl
Cu	0.09	0.15	0.10	0.12	0.05	0.07	0.08	0.09	0.07	0.27
Ni	bdl	bdl	bdl	bdl	bdl	0.04	0.03	0.02	0.03	0.55
Co	0.05	0.05	0.06	0.03	0.06	0.04	0.10	0.11	0.10	bdl
Fe	60.96	61.23	61.04	59.99	60.19	60.06	60.25	60.42	60.18	59.07
Mn	0.04	0.03	0.03	bdl	bdl	bdl	0.03	0.03	0.04	bdl
Total	99.46	100.03	99.82	98.48	98.48	99.23	99.68	99.92	99.81	98.18
S (at.%)	52.163	52.228	52.330	52.618	52.432	53.004	53.000	52.982	53.146	52.704
As	0.020	0.000	0.000	0.000	0.000	0.000	0.000	0.000	0.000	0.000
Cu	0.063	0.099	0.066	0.084	0.036	0.051	0.057	0.064	0.050	0.190
Ni	0.000	0.001	0.002	0.000	0.000	0.026	0.024	0.014	0.023	0.410
Co	0.033	0.040	0.041	0.025	0.043	0.033	0.075	0.083	0.075	0.001
Fe	47.690	47.611	47.534	47.274	47.489	46.887	46.818	46.834	46.674	46.695
Mn	0.031	0.022	0.027	0.000	0.000	0.000	0.026	0.023	0.032	0.000

n = number of analyses averaged; bdl = below detection limit; incl = inclusion; py = pyrite; Se, Pb = bdl.

Table 4
Compositions of chalcopyrite.

Analysis no.	MF1-928b-21	MF1-928b-22	MF1-928b-102	MF1-928b-101	SV3.2353.7	SV3.2353.1	SV3-2353a.23	SV3-2353a.22
Size	5 μm	15 μm	8 μm	5 μm	40 μm	8 μm	9 μm	12 μm
Comment	Subhedral	Subhedral	Euhd incl in cal	Euhd incl in cal	Anhedral	Subhedral	Subhedral	Subhedral
n=	1	1	1	1	3	1	1	1
S (wt%)	34.69	34.34	34.16	33.96	34.45	34.38	34.13	34.04
Cu	35.08	34.96	34.93	34.99	35.04	33.78	35.05	35.27
Ni	0.00	0.00	0.05	0.05	0.27	0.17	0.41	0.29
Zn	0.00	0.00	0.09	0.08	0.10	0.14	0.00	0.00
Co	0.00	0.00	0.20	0.00	0.00	0.05	0.00	0.00
Fe	28.69	29.65	29.65	29.61	30.25	30.20	29.86	29.76
Total	98.46	98.95	99.08	98.69	100.12	98.70	99.45	99.36
S (at.%)	50.372	49.766	49.513	49.441	49.430	49.86	49.33	49.27
Cu	25.706	25.565	25.548	25.709	25.365	24.72	25.56	25.76
Ni	0.000	0.000	0.040	0.040	0.210	0.13	0.32	0.23
Zn	0.000	0.000	0.064	0.057	0.074	0.10	0.00	0.00
Co	0.000	0.000	0.158	0.000	0.000	0.04	0.00	0.00
Fe	23.923	24.670	24.678	24.753	24.921	25.15	24.78	24.74

bdl = below detection limit; incl = inclusion; cal = calcite; euhd = euhedral; n = number of analyses averaged; Pb, Se = bdl.

Arsenopyrite crystals in sample MF5–2605 were either euhedral or subhedral; however, all the inner, low Co zones, were euhedral with a sharp boundary separating the low Co portion from the higher Co outer portion (Fig. 4A, B). All the inner low Co areas were inclusion rich relative to the outer high Co areas. Alkali and plagioclase feldspar and quartz inclusions were identified by EDS; some inclusions were empty and are probable fluid inclusions intersected by the thin section surface. Roedder (1984) suggests that such inclusion textures indicate rapid growth, hence trapping solids and fluids.

Although the ideal formula of arsenopyrite is FeAsS, the chemistry of naturally occurring phases varies from $FeAs_{0.9}S_{1.1}$ to $FeAs_{1.1}S_{0.9}$ where the ratio of Fe:(As + S) is 1:2 (Morimoto and Clark, 1961; Kerestedjian, 1997). This variation is a systematic effect of changes in temperature and pressure of formation. Arsenopyrite typically contains Co and forms a series with glaucodot ((Co, Fe)AsS). Arsenopyrites in Mofete sample MF5–2605 have S > As and the formula is $FeAs_{0.9}S_{1.1}$. Co is enriched in the rims, producing the observed zoning (Table 7). Co varies from 1.72 to 0.06 wt%, Ni varies from 0.60 to 0.05 wt%, and Se, Cu and Mn were detected in minor abundance usually at dl or 2 or 3 times dl. Au and Pb were not detected. Table 7 gives representative compositions of arsenopyrite.

5.7. *Nickel sulfides*

Nickel sulfides were rare and only identified in three samples (Table 1). Between two pyrrhotite grains in sample MF5–2605, we identified one small (~2 μm) millerite (NiS) grain by EDS. The other two occurrences were both from the San Vito 3 core, but the single grain in SV3–2105 was too small for EPMA. The Ni-sulfide grains in SV3–2353 varied from anhedral, subhedral, to euhedral and all were in epidote or clinozoisite. One large grain (30 μm) was mottled and had an attached small grain (20 μm) that appeared altered (Fig. 4D); we analyzed the higher Z part of the two grains. The other grains in sample SV3–2353 were not mottled, appeared unaltered, and were euhedral or subhedral, thus we assume they are authigenic (e.g., Fig. 4E).

The thiospinel violarite, ideally $Fe^{2+}Ni_2^{3+}S_4$, has a large range of composition with the Fe:Ni ratio highly variable. Fe + Ni typically is >3 and sulfur is commonly deficient (e.g., Misra and Fleet, 1974; Vaughan

Table 5
Compositions of sphalerite.

Analysis no.	MF1-1150.12	MF1-1150.17	MF1-1150.25	MF1-1150.7	MF1-1150.13	MF1-1150a.101	MF1-1150.20	MF2-1715.101	MF2-1715.102	SV1-2125.5	SV1-2125.10
Size	40 μm	60 μm	30 μm	15 μm	30 μm	20 μm	15 μm	15 μm	16 μm	3 μm	80 μm
Comment	Subhedral	Subhedral	Subhedral	Euhd in vug	Anhedral	Euhedral	Subhedral	Euhedral	Euhedral	Incl in py	Anhedral
n=	3	2	2	1	1	1	1	1	1	1	3
S (wt%)	32.36	32.56	31.79	30.76	33.25	32.45	32.33	32.86	34.15	33.10	33.34
Se	0.02	bdl	0.03	bdl	bdl	bdl	bdl	bdl	bdl	bdl	bdl
Zn	63.08	63.86	62.03	58.51	64.65	61.42	62.68	50.67	52.67	59.24	64.96
Cu	1.04	0.89	1.48	0.13	0.78	0.51	0.30	0.02	0.02	2.99	bdl
Fe	2.89	2.49	3.67	1.78	2.29	2.67	3.4	11.40	11.85	2.91	2.93
Mn	0.24	0.23	0.17	bdl	bdl	0.27	0.16	0.45	0.47	bdl	bdl
Cd	bdl	bdl	bdl	bdl	bdl	0.18	0.18	0.07	0.07	bdl	bdl
Total	99.62	100.04	99.18	91.18	100.97	97.50	99.05	95.47	99.23	98.23	101.25
S (at.%)	49.322	49.421	48.786	50.814	49.884	50.261	49.502	50.913	50.907	50.669	49.855
Se	0.008	0.000	0.021	0.000	0.000	0.000	0.000	0.000	0.000	0.000	0.000
Zn	47.135	47.527	46.669	47.385	47.552	46.642	47.055	38.491	38.495	44.467	47.624
Cu	0.801	0.680	1.146	0.112	0.589	0.399	0.232	0.016	0.015	2.308	0.006
Fe	2.529	2.171	3.230	1.688	1.975	2.375	2.989	10.142	10.143	2.556	2.514
Mn	0.214	0.202	0.148	0.000	0.000	0.244	0.143	0.407	0.409	0.000	0.000
Cd	0.000	0.000	0.000	0.000	0.000	0.080	0.079	0.031	0.030	0.000	0.000
mole% FeS	5.0	4.3	6.3	3.4	3.9	4.8	5.9	20.7	20.7	5.2	5.0

n = number of analyses averaged; bdl = below detection limit; incl = inclusion; py = pyrite; euhd = euhedral; Pb, As = bdl.

Table 6
Representative compositions of galena.

Analysis no.	MF1-1150.21	MF1-1495.10	SV1.2125.3	SV1-2125.12	SV1-2125.7	SV1-2125.11a	SV1-2125b.1	SV3-2353.5
Size	30 μm	3 μm	5 μm	6 μm	4 μm	10 μm	10 μm	4 μm
Comment	Subhedral	Incl in py	Subhedral	Subhedral	Incl in py	Subhedral	Incl in py	Euhedral
n=	1	1	2	3	1	1	1	1
S (wt%)	12.66	13.36	13.41	13.48	13.45	13.19	12.68	13.36
Se	bdl	0.10	bdl	0.03	bdl	0.03	bdl	0.12
Cu	0.02	0.04	0.14	0.09	0.03	0.05	bdl	0.13
Fe	0.92	bdl	0.07	bdl	0.04	0.29	0.88	bdl
Ag	bdl	bdl	bdl	bdl	bdl	bdl	0.05	0.07
Pb	81.03	86.24	87.15	87.29	87.28	87.68	86.19	86.72
Cd	bdl	bdl	0.09	0.14	bdl	bdl	bdl	0.11
Total	94.63	99.73	100.95	101.06	100.80	101.24	99.80	100.54
S (atomic %)	49.184	49.917	49.603	49.764	49.825	48.913	47.776	49.575
Se	0.000	0.147	0.000	0.047	0.000	0.041	0.000	0.178
Cu	0.045	0.072	0.255	0.166	0.050	0.101	0.000	0.247
Fe	2.046	0.000	0.141	0.000	0.084	0.607	1.904	0.000
Ag	0.000	0.000	0.000	0.000	0.000	0.000	0.056	0.078
Pb	48.725	49.863	49.910	49.878	50.038	50.339	50.264	49.804
Cd	0.000	0.000	0.091	0.143	0.000	0.000	0.000	0.119

n = number of analyses averaged; bdl = below detection limit; incl = inclusion; py = pyrite; Sb, Mn = bdl.

and Craig, 1985). Desborough and Czamanske (1973) have suggested that the stoichiometry of violarite should be (Fe, Ni)$_9$S$_{11}$, although Misra and Fleet (1974) and Vaughan and Craig (1985) do not support this argument. Only one analyzed grain (Table 8) has a stoichiometry of M_3S_4, the others vary from $M_{3.44}S_4$ to $M_{3.63}S_4$. We have tentatively identified these Ni-bearing sulfides as violarite. Violarite is commonly found as an alteration product of pentlandite in hydrothermal environments (e.g., Misra and Fleet, 1974; Tenailleau et al., 2006). The two grains shown in Fig. 4D could be from altered magmatic pentlandite, although we are unaware of pentlandite described in the Campi Flegrei volcanic products. Table 8 gives the compositions of these Ni, Fe sulfides.

5.8. Acanthite

In five samples from three wells (Table 1), we identified a late-stage silver sulfide by EDS. In all occurrences, the habit was arborescent, thorn-shaped masses (Fig. 4F), some as large as 70 μm, but all unpolished and in cracks, or vugs. We used the AZtec Oxford EDS software to obtain compositions and they all appeared to have the same composition and relative Ag and S spectra peak heights. Two analyses from sample MF2–1824 yielded Ag 87.02, S 12.98 wt%, which calculates to Ag 66.6, S 33.4 atomic % compatible with Ag_2S. No other elements ≥0.5 wt% were detected.

Monoclinic acanthite (α-Ag_2S) is paramorphic with isometric argentite (β-Ag_2S) with the transition between the higher temperature argentite and the lower temperature acanthite at 176.85 °C (Sadovnikov and Gusev, 2019). Hence, all Ag_2S at room temperature is acanthite. We could not determine crystal shape; however, considering the measured well temperatures (Table 1), we assume that the initial phase was argentite (β-Ag_2S).

Table 7
Representative compositions of arsenopyrite.

Analysis no.	Zoned		Zoned		Zoned		MF5-2605.12	MF5-2605.6a	MF5-2605.7a	MF1-1398.1
	MF5-2605.5r	MF5-2605.5c	MF5-2605.8r	MF5-2605.8c	MF5-2605.15r	MF5-2605.14c				
Size	80 μm	80 μm	40 μm	40 μm	80 μm	80 μm	100 μm	65 μm	55 μm	8 μm
Comment	Euhedral rim	Euhedral core	Subhedral rim	Euhedral core	Euhedral rim	Euhedral core	Euhedral	Euhedral	Euhedral	Incl in py
n=	1	2	1	1	1	1	3	1	1	1
S (wt%)	20.11	21.14	21.18	20.50	20.54	20.07	20.25	20.935	20.363	21.49
As	44.48	42.39	42.75	43.83	44.31	44.53	44.36	43.32	44.39	43.76
Se	bdl	bdl	0.04	0.04	0.06	0.04	0.04	bdl	bdl	bdl
Cu	bdl	bdl	0.02	0.02	bdl	bdl	0.02	bdl	bdl	bdl
Ni	0.23	0.23	0.60	0.05	0.22	0.06	0.19	0.06	0.22	0.07
Co	1.09	0.10	1.72	0.26	1.47	0.26	0.97	0.97	1.21	0.20
Fe	33.74	35.55	33.47	34.93	33.42	33.24	33.71	34.59	33.92	34.48
Mn	bdl	0.02	bdl	bdl	0.02	bdl	bdl	0.07	0.09	0.03
Total	99.65	99.43	99.77	99.58	100.04	98.20	99.53	99.95	100.19	100.03
S:As	1.06	1.15	1.16	1.09	1.08	1.05	1.07	1.13	1.07	1.15
S (at.%)	33.946	35.290	35.309	34.447	34.432	34.361	34.174	34.925	34.125	35.706
As	32.137	30.295	30.503	31.524	31.798	32.637	32.048	30.938	31.840	31.123
Se	0.000	0.000	0.027	0.029	0.039	0.025	0.030	0.000	0.000	0.000
Cu	0.000	0.000	0.013	0.015	0.000	0.000	0.014	0.000	0.000	0.000
Ni	0.212	0.210	0.547	0.046	0.202	0.056	0.175	0.058	0.203	0.064
Co	1.001	0.090	1.560	0.235	1.341	0.242	0.887	0.879	1.107	0.181
Fe	32.704	34.085	32.040	33.704	32.170	32.678	32.672	33.134	32.638	32.897
Mn	0.000	0.019	0.000	0.000	0.019	0.000	0.000	0.066	0.087	0.029

n = number of analyses averaged; bdl = below detection limit; incl = inclusion; py = pyrite; Pb, Au = bdl.

Table 8
Compositions of violarite.

	1	2	3	4	5	6	7	8
Analysis no.	SV3-2353.9	SV3-2353.10	SV3-2353.115	SV3-2353.117	SV3-2353a.Ni3	SV3-2353.111	SV3-2353a.5	SV3-2353.113
Size	30 μm	20 μm	35 μm	10 μm	10 μm	20 μm	4 μm	8 μm
Comment	Anhedral	Anhedral	Euhedral	Euhedral	Subhedral	Subhedral	Euhedral	Euhedral
n=	2	1	1	1	1	1	1	1
S (wt%)	40.94	38.43	37.90	39.03	38.59	39.22	37.96	39.00
As	bdl	bdl	0.31	0.30	bdl	bdl	bdl	0.29
Cu	0.46	0.18	0.18	0.24	0.15	0.32	bdl	0.21
Ni	41.53	50.48	47.23	15.07	20.57	7.18	45.91	14.86
Zn	bdl	bdl	0.04	0.04	bdl	bdl	bdl	bdl
Co	1.65	0.07	1.90	0.25	0.23	0.26	1.39	0.26
Fe	13.06	9.29	12.88	45.13	39.41	52.99	12.63	44.77
Total	97.64	98.44	100.44	100.06	98.95	99.97	97.89	99.39
S (at.%)	56.657	53.769	52.362	53.041	53.110	53.090	53.423	53.279
As	0.000	0.000	0.183	0.175	0.000	0.000	0.000	0.170
Cu	0.322	0.125	0.125	0.165	0.104	0.219	0.000	0.145
Ni	31.402	38.590	35.656	11.191	15.469	5.311	35.306	11.093
Zn	0.000	0.000	0.027	0.027	0.000	0.000	0.000	0.000
Co	1.240	0.051	1.429	0.185	0.172	0.192	1.065	0.193
Fe	10.379	7.465	10.218	35.217	31.145	41.189	10.207	35.120

n = number of analyses averaged; bdl = below detection limit; Se = bdl.
1 - (Fe, Co, Cu, Ni)Σ3.06 (S)4.
2 - (Fe, Co, Cu, Ni)Σ3.44 (S)4.
3 - (Fe, Co, Cu, Zn,Ni)Σ3.63 (As+S)4.01.
4 - (Fe, Co, Cu, Zn,Ni)Σ3.53 (As+S)4.01.
5 - (Fe, Co, Cu, Ni)Σ3.53 (S)4.
6 - (Fe, Co, Cu, Ni)Σ3.53 (S)4.
7 - (Fe, Co, Ni)Σ3.49 (S)4.
8 - (Fe, Co, Cu, Ni)Σ3.50 (As+S)4.01.

5.9. Bismuth phases

We identified two late-stage bismuth minerals in samples MF5–2610 and SV1–2860. All the grains were either too small and/or unpolished in cracks, which precluded EPMA experiments. We used AZtec Oxford EDS software to obtain compositions. One grain in SV1–2860 and three in MF5–2610 (Fig. 4G) appeared to be native bismuth with no other element $\geq$0.5 wt%. Sample MF5–2610 also contained 12 grains of a bismuth telluride, some as large as 9 μm (Fig. 4H), but unpolished and in cracks. Using the AZtec EDS system we obtained the following composition ($n = 3$) Bi 51.8, Te 48.2 wt%, which calculates to Bi 39.6, Te 60.4 atomic %; no other element ≥0.5 wt% was detected. This is compatible with tellurobismuthite (Bi_2Te_3). Furthermore, some grains showed a platy habit (Fig. 4H) characteristic of some tellurobismuthite occurrences (Anthony et al., 2023).

5.10. Scheelite

We identified scheelite ($Ca(WO_4)$) in both the Mofete and San Vito cores, but only in the San Vito 3 well was it abundant. In the MF1 well, it was a late-stage mineral occurring in vugs (Fig. 5A), associated with calcite (Fig. 5B), and with fluorite (Fig. 5C); its habit was subhedral, but most often anhedral filling spaces between earlier phases. It was rare and too small in well MF5 for EPMA and not identified in MF2 (Table 1). In the SV1–2125 sample, scheelite grains were small, often associated with fluorite, and not amenable for EPMA. In the lower portion of SV1, sample SV1–2860, two relatively large amoeboid-shaped scheelite grains in alkali and plagioclase feldspar had feldspar inclusions. Scheelite was common in the three SV3 samples, but in SV3–2105 the scheelite grains were too small or in cracks and not amenable for EPMA. Scheelite was abundant in SV3–2353 (Fig. 5D) and somewhat less so in sample SV3–2359. In those two samples, late-stage scheelite filled spaces between diopside, titanite, meionite, and alkali and plagioclase feldspar.

In preparation for EPMA experiments on scheelite, we ran WDS scans and did not observe peaks indicative of rare earth elements (REEs) or Y in those wavelength scans. Laser ablation inductively coupled mass spectrometry (LA-ICP-MS) would be the technique of choice for determining low amounts of REE + Y, but was not available for this study.

Tetragonal scheelite ($Ca(WO_4)$) and powellite ($Ca(MoO_4)$) form an isostructural binary solid-solution series where W^{6+} substitutes for Mo^{6+}. Hazen et al. (1985) report very small differences (<1 %) in unit cell parameters, such that miscibility should be common where both ion species are available. Scheelite analyzed in MF1 is unzoned in BSE images, but has a Mo^{6+} content that varies from dl to 4.8 mol% $Ca(MoO_4)$; WO_3 varies from 77.10 to 79.25, MoO_3 varies from dl–2.43, and CaO varies from 19.28 to 20.20 wt%. Other minor detected elements are (in wt%) Na_2O dl–0.11, FeO as total iron dl–1.01, MgO 0.04–0.14, Al_2O_3 dl–0.10, and MnO dl–0.08. The two scheelite grains in sample SV1–2860 are unzoned and close to stoichiometric $Ca(WO_4)$ (0.0 and 0.2 mol% $Ca(MoO_4)$). Scheelite in SV3–2353 has widely variable Mo^{6+} content that varies from 0.0 to 9.8 mol% $Ca(MoO_4)$ and is complexly zoned. Fig. 5E shows a typical example of the irregular, patchy zoning; Table 9 gives the complete analysis of the marked points. We suggest that all of the scheelite in sample SV3–2353 may be zoned, but only displays zoning as a function of how the thin section surface cuts the grain. Scheelite in sample SV3–2359 is zoned, but with much less Mo^{6+}; mole% $Ca(MoO_4)$ varies from 0.2 to 1.0. Analyses of SV3–2353 and SV3–2359 yield, in wt %, CaO 19.32–20.30, WO_3 73.68–81.93, MoO_3 dl–4.98, Na_2O dl–0.28, FeO as total iron dl–0.83, MgO dl–0.19, Al_2O_3 dl-0.36, and MnO dl–0.05. Table 9 gives representative compositions for scheelite.

During SEM scans using a Hitachi UVD CL detector, we noted that scheelite is intensely CL active, but we could not discern differences in color. Fig. 5F shows an RGB-filtered CL image obtained with a Delmic SPARC CL detector at an exposure time of 59.3 μs/pixel. Note that the colors correlate with the composition as shown in Fig. 5E. Low values of MoO_3 are in shades of blue, whereas higher values are in yellows, oranges, and browns. Also reflected in the color variability is the complexity of zoning as shown with BSE imaging. However, the CL shows more complex zoning. Poulin et al. (2016) studied the correlation of CL color response with composition using LA-ICP-MS to obtain Mo, As, Sr, and ΣREE+Y compositions of scheelite from geologically diverse ore-deposit environments. They found that only the Mo concentration was correlatable with color; variations in the other measured elements produced no effect in CL response.

Table 9
Representative compositions of scheelite.

Analysis no.	MF1-1150.1	MF1-1398.3	MF1-1495.12	SV1-2860.1	SV3-2353.1	SV3-2353.2	Zoned				Zoned	
							SV3-2353.10b	SV3-2353.12b	SV3-2353.11b	SV3-2353.13b	SV3-2359.7	SV3-2359.8
Size	12 μm	30 μm	15 μm	75 μm	30 μm	25 μm	65 μm	65 μm	55 μm	25 μm	50 μm	50 μm
Comment	Subhedral	Anhedral	Euhedral	Anhedral	Euhedral	Anhedral	Anhedral	Anhedral	Anhedral	Anhedral	Subhedral	Subhedral
n=	1	1	1	1	1	1	1	1	1	1	1	1
Na_2O (wt%)	bdl	0.03	0.04	bdl	0.02	bdl	bdl	bdl	bdl	bdl	bdl	0.28
CaO	19.45	20.20	19.28	19.32	20.00	19.64	19.63	19.69	19.63	20.01	19.59	19.78
FeO*	0.26	bdl	0.75	0.04	0.03	0.05	bdl	0.07	0.08	0.03	0.15	0.08
MgO	0.04	0.10	0.05	bdl	bdl	bdl	bdl	0.06	0.04	0.07	bdl	bdl
Al_2O_3	0.09	bdl	0.08	bdl	bdl	bdl	bdl	bdl	bdl	bdl	bdl	bdl
WO_3	79.25	77.98	77.27	79.61	76.80	81.93	78.35	76.21	78.66	73.68	81.26	79.51
MoO_3	bdl	2.43	0.28	0.09	2.54	bdl	0.56	2.98	1.27	4.98	0.08	0.51
MnO	0.03	bdl	bdl	bdl	0.02	0.02	bdl	bdl	bdl	bdl	0.04	0.02
Total	99.12	100.74	97.75	99.06	99.41	101.64	98.54	99.01	99.68	98.77	101.11	100.19
Formulae on the basis of 4 oxygens												
Na	0.000	0.003	0.004	0.000	0.002	0.000	0.000	0.000	0.000	0.000	0.000	0.026
Ca	1.005	1.012	1.008	1.001	1.016	0.993	1.018	1.002	1.002	1.008	0.994	1.009
Fe^{2+}	0.010	0.000	0.031	0.002	0.001	0.002	0.000	0.003	0.003	0.001	0.006	0.003
Mg	0.003	0.007	0.004	0.000	0.000	0.000	0.000	0.004	0.003	0.005	0.000	0.000
Al	0.005	0.000	0.005	0.000	0.000	0.000	0.000	0.000	0.000	0.000	0.000	0.000
W	0.991	0.946	0.977	0.997	0.943	1.002	0.983	0.938	0.972	0.898	0.998	0.981
Mo	0.000	0.047	0.006	0.002	0.050	0.000	0.011	0.059	0.025	0.098	0.002	0.010
Mn	0.001	0.000	0.000	0.000	0.001	0.001	0.000	0.000	0.000	0.000	0.002	0.001
Total	2.02	2.02	2.03	2.00	2.01	2.00	2.01	2.01	2.01	2.01	2.00	2.03
$Ca(WO_4)$ (mol.%)	100.0	95.2	99.4	99.8	94.9	100.0	98.9	94.1	97.5	90.2	99.8	99.0
$Ca(MoO_4)$	0.0	4.8	0.6	0.2	5.1	0.0	1.1	5.9	2.5	9.8	0.2	1.0

n = number of analyses averaged; FeO* = total iron as FeO; bdl = below detection limit; Si, Sr = bdl.

5.11. Molybdenite

Molybdenite was observed in only two samples from the San Vito wells, SV1 and SV3 (Table 1). In all cases, they were late stage, commonly in vugs, and all had a blade shape (Fig. 5G). None were amenable for EPMA experiments, but were identified by EDS. We did not find any elements ≥0.5 wt% other than Mo and S.

5.12. Cassiterite

Only three grains, from 2 to 3 μm in size, of cassiterite were identified by EDS (Table 1). Their occurrence in vugs and cracks suggests that they are a rare late-stage authigenic phase. EDS spectra did not yield any elements ≥0.5 wt% aside from Sn and O.

6. Discussion

6.1. Distribution of mineralization

Table 1 gives the occurrence of the various minerals as identified with EPMA or EDS. A caveat to this distribution table is that a typical petrographic thin section (46 mm × 26 mm × 30 μm) may not give representative sampling in geothermal systems at any particular depth. Geothermal systems typically are highly fractured and brecciated (e.g., Hulen and Nielson, 1987; Watanabe and Takahashi, 1995; Fischer et al., 2003; Hanano, 2004; Wang et al., 2020) such that the mineral deposition maybe irregular or isolated in veins or in their proximity. Gaps in the distribution such as the absence of galena in SV1–2510 or SV3–2105, we do not think are significant. However, we believe that the absence of arsenopyrite in the San Vito wells, and the absence of pyrrhotite in the MF1 well and upper part of the SV1 well are significant and reflect on the depositional pressure, temperature, and chemical (*PTX*) conditions.

6.2. Environment of ore deposition

Since the end of World War II, there have been, at least, a thousand or more experimental studies on various sulfide systems at different *PTX* conditions. Reports on the various phase-intensive parameter relationships have been from equilibrium-assumed experiments. Barton Jr. (1991) warns us that for the successful application of any sulfide experiment to a natural system, one must be able to prove textural equilibrium between or among the phases. However, we have not observed any convincing textural equilibrium in either the San Vito or Mofete samples, except on a very local scale. For example, in some samples, we see pyrite later than pyrrhotite or sulfides in the cracks of earlier phases. We also note that accompanying silicates, such as the epidote supergroup (Belkin and De Vivo, 2023) are pervasively zoned. However, the absence of pyrrhotite in the MF1 well and in the upper part of the SV1 suggests higher log fS_2 conditions relative to pyrrhotite stability such that pyrite is the stable phase. Studies of pyrite-pyrrhotite equilibria (e.g., Barker and Parks, 1986 and references therein) show that pyrite is favored by higher sulfur activity at the well temperatures of the studied Mofete and San Vito samples. Thus, we assume that the absence of pyrrhotite in MF1 and in the upper part of the SV1 samples is due to higher sulfur activity. Although, in terms of sulfidation state (e.g., Einaudi et al., 2003; Fontboté et al., 2017), both the Mofete and San Vito wells would be classified as low sulfidation.

Arsenic in pyrite is common in all Mofete well pyrite and ranges from dl to 4.89 wt%, but is rare in the San Vito well pyrites; As was only detected in four San Vito pyrite grains and just at the detection limit. Arsenopyrite was identified in the MF1, MF2, and MF5 wells, abundant in sample MF5–2605, but not detected in either SV1 or SV3. Various studies (e.g., Kretschmar and Scott, 1976; Pokrovski et al., 2002) on the formation of arsenopyrite in sulfide- bearing hydrothermal systems suggest that the *PT* conditions were appropriate for arsenopyrite formation in the SV1 and SV3 wells.

Guglielminetti (1986) reports for the Mofete wells that the sampled fluid arsenic composition calculated at reservoir conditions was 9 ppm in MF1 (550–896 m), 11 ppm in MF1 (1273–1606 m), and 11 ppm in MF2 (1275–1989 m). The As fluid composition in MF5 (2310–2699 m) was not determined. Bruni et al. (1985) give a partial analysis of fluids sampled during purge tests of San Vito 1 well, but did not analyze for As. De Vivo et al. (2011) and Albanese et al. (2023) indicate that, in general, the Campi Flegrei soils are enriched in As and Aiuppa et al. (2006) report that the As content of groundwaters sampled in the Campi Flegrei area varies from 1.6 to 6900 μg/l, which was similar to the results of Celico et al. (1992) for a 20 year (1970–1990) monitoring of wells and springs from the Campi Flegrei area. Valentino and Stanzione (2003) analyzed 4 pumped well water samples from the San Vito area, that varied from 20 to 43 μg/l As, which were among the lowest values they obtained for samples from wells, springs, and pools. It appears from our literature survey that the As content of fluids in the Campi Flegrei area varies at least four orders of magnitude. We do not have any direct data for the As concentration in fluids encountered during drilling of the SV1 and SV3 wells. However, we think it is reasonable to suggest that the absence of arsenopyrite in those wells is a result of a low concentration of As in the geothermal fluid.

Tungsten in most hydrothermal/geothermal or ore-forming environments occurs as W^{6+} even in moderately reducing environments (Che et al., 2013); however, molybdenum can occur as either Mo^{6+} or Mo^{4+} as a function of oxygen fugacity. The Mo^{6+} species can substitute for W^{6+} in the scheelite structure. Under reducing conditions Mo^{4+} can form molybdenite as a function of sulfur fugacity if sulfur is present in the fluid. We identified both Mo-bearing scheelite and molybdenite in samples SV1–2860 and SV3–2353 and scheelite in sample SV3–2353 is strongly zoned (Fig. 5E, F) in MoO_3.These occurrences attest to the variability of fO_2 and fS_2 in the geothermal fluid. This fO_2 variability is compatible with the origin of the zoning observed in the epidote supergroup minerals described in the same samples by Belkin and De Vivo (2023).

6.3. Geothermal ore-mineral occurrence

Ore minerals such as pyrite, pyrrhotite, chalcopyrite, sphalerite, and galena, are very commonly identified during drilling of geothermal fields (Skinner et al., 1967; McKibben and Elders, 1985; McKibben et al., 1988) and in sulfide-rich scale formed in pipes transmitting high enthalpy fluids to power plants (e.g., Hardardóttir et al., 2005; Raymond et al., 2005; Harijoko et al., 2015). The other minerals identified in the Mofete and San Vito wells have various levels of abundance in modern geothermal systems. Ballantyne and Moore (1988) indicate that most geothermal systems are undersaturated with respect to arsenopyrite and that its occurrence is uncommon, although Bundschuh and Maity (2015) indicate arsenopyrite is the dominant As-bearing mineral at temperatures >250 °C. We found arsenopyrite throughout the Mofete 1, 2 and 5 wells, from 255 to 350 °C and, except for sample MF5–2605, it was not abundant. Arsenopyrite has been identified from a few other geothermal fields (Browne, 1984; Goff and Gardner, 1994). Native bismuth and bismuth tellurides are not common geothermal minerals, although geothermal fluids may have relatively high concentrations especially of tellurium (Simmons and Kirby, 2020). Native bismuth has been reported as inclusions in sphalerite (Daliran, 2008). Silver, Au, and Pb tellurides have been reported from various geothermal fields (e.g., Daliran, 2008; Ward et al., 2006). Tellurides are commonly associated with gold-bearing fossil geothermal/epithermal deposits (e.g., Pals and Spry, 2003); however, we are unaware of any modern geothermal tellurobismuthite occurrence. Silver-bearing minerals and native silver are common in geothermal fields (e.g., Goff and Gardner, 1994; Ward et al., 2006; Reich et al., 2020; Grant et al., 2020) and acanthite (or argentite) has been reported from geothermal fields (e.g., Krupp and Seward, 1987; Raymond et al., 2005; Reich et al., 2020). Ni-bearing minerals are rare in geothermal fields. However, Browne (1969, 1984) reports Ni-rich glaucodot as exsolution in sphalerite and rare pentlandite, both from the Broadlands geothermal field and Reyes et al. (2002) identified millerite and pentlandite from mineral deposits in the Rotokawa geothermal pipelines, New Zealand. Geothermal cassiterite is rare, but it has been reported from the Tauhara Geothermal Field, NZ (Kakimoto and Browne, 1986). A poorly crystalline molybdenite has been reported from the Valles caldera, New Mexico geothermal system (Hulen et al., 1987; Goff and Gardner, 1994).

Tungsten concentrations have been measured in many geothermal fluids. For example, Guo et al. (2019) report very high values up to 1103 μg/l W in the Tibet geothermal province, China, and Zhao et al. (2021) report concentrations up to 78 μg/l W in the Rehai geothermal area, China. In all cases in modern geothermal systems, we are unaware of scheelite reported as an authigenic mineral. However, in ancient porphyry/epithermal/geothermal systems, especially related to Au occurrences, scheelite is a common phase (e.g., Schenk and Höll, 1991; Milési et al., 1994; Grancea et al., 2002).

Choi and Youm (2000) describe the Ulsan scheelite-bearing skarn deposit as genetically related to a low-sulfidation porphyry system. The Ulsan deposit has similar element and mineral associations that we found in the Campi Flegrei geothermal system, scheelite, Bi, Ag, and Ni minerals, pyrrhotite, and arsenopyrite. This suggests that the environment of deposition of the ore mineral assemblage that we identified in the Campi Flegrei geothermal field is similar to a low-sulfidation porphyry system as described by Choi and Youm (2000).

Wang et al. (2021) investigated experimentally the solubility of W^{6+} species in fluorine-rich aqueous fluids to model granite-fluid interaction. They found that the W^{6+} solubility was increased significantly in F-bearing solutions at vapor-saturated conditions between 100 and 250 °C. We identified common fluorite (e.g., Figs. 3E, 5C) and fluorapatite in both the Mofete and San Vito samples. This suggests that the ability of the Campi Flegrei geothermal fluids to carry W species was likely enhanced by the fluorine content of the fluids. Unfortunately, the only measurement of the F content during Mofete or San Vito drilling is by Bruni et al. (1985) who gives the value of 5 ppm F in fluids sampled during purge tests in SV1. Wang et al. (2023) investigated the control of Ca-bearing mineral (fluorite and apatite) precipitation during W-bearing ore-fluid transport to form W ore deposits. They suggest that major ferberite ($Fe^{2+}(WO_4)$) ore deposits are the result of the removal of Ca from the W-bearing solutions by fluorite and/apatite precipitation such that scheelite does not form. In contrast, the geothermal fluids in both the Mofete and San Vito fields had sufficient Ca^{2+} such that Ca-bearing mineral (e.g., epidote supergroup, diopside, titanite, fluorite, and apatite) formation did not interfere with scheelite deposition.

7. Summary

Geothermal fluids in the Mofete and San Vito fields, Campi Flegrei volcanic complex, west of Naples, Italy, have precipitated various authigenic ore minerals. Sulfides, oxides, native elements, tungstates, and tellurides have been identified in the MF1, MF2, and MF5 wells from the Mofete field, and in the SV1 and SV3 wells from the San Vito field. The distribution of the ore mineralization is controlled mainly by sulfur activity and the availability of ionic species in the fluids. The mineral assemblage indicates a low sulfidation environment. Scheelite was identified in both the Mofete and San Vito wells, but was more abundant in the SV3 well. In the SV3 well, scheelite is zoned with variable Mo^{6+} and the compositional zoning is reflected in different cathodoluminescence, blue in low Mo^{6+} zones, yellow to brown in high Mo^{6+} zones. The occurrence of Mo-bearing scheelite and MoS_2 in the same sample indicates the variability of fO_2 and fS_2 in the geothermal fluid.

CRediT authorship contribution statement

Harvey E. Belkin: Writing – review & editing, Writing – original draft, Methodology, Formal analysis, Data curation, Conceptualization. **Ryan J. McAleer:** Writing – review & editing, Formal analysis. **Benedetto De Vivo:** Resources.

Declaration of competing interest

The authors declare that they have no known competing financial interests or personal relationships that could have appeared to influence the work reported in this paper.

Data availability

All data in supplemental tables

Acknowledgments

We thank the Agip–Enel Joint Venture for permission to use the samples facilitated by Walter Chelini. We thank Giuseppe Cavarretta (CNR Roma Ret.) for valuable discussions on authigenic mineral formation in geothermal systems. Reviews by Nora K. Foley and Nadine Piatak-Hackley (both U.S. Geological Survey) greatly improved the manuscript. We thank two anonymous reviewers for their helpful and constructive comments. We especially thank Mary R. Croke (U.S. Geological Survey) for creating the Data Release related to this publication.

Disclaimer

Any use of trade, product, or firm names is for descriptive purposes only and does not imply endorsement by the United States government.

Appendix A. Supplementary data

Supplementary data to this article can be found online at https://doi.org/10.1016/j.gexplo.2024.107556.

References

Aiuppa, A., Avino, R., Brusca, L., Caliro, S., Chiodini, G., D'Alessandro, W., Favara, R., Federico, C., Ginevra, W., Inguaggiato, S., Longo, M., 2006. Mineral control of arsenic content in thermal waters from volcano-hosted hydrothermal systems: insights from island of Ischia and Phlegrean Fields (Campanian Volcanic Province, Italy). Chem. Geol. 229, 313–330.

Albanese, S., Ebrahimi, P., Aruta, A., Cicchella, D., De Vivo, B., Lima, A., 2023. Potentially toxic elements in the soils of Campi Flegrei (south Italy) and the immediate surroundings: Spatial distribution, origin, and probabilistic human health risk. Chemosphere 313, 137297. https://doi.org/10.1016/j.chemosphere.2022.137297.

Altaner, S.P., Lander, R.H., Klimentidis, R.E., and Ylagan, R.F., 1991. Hydrothermal alteration in two active geothermal wells from the Phlegrean volcanic fields, Italy. 28th Annual Clay Minerals Society Meeting, Houston, TX, 5–10 Oct., 28,4.

Anthony, J.W., Bideaux, R.A., Bladh, K.W., Nichols, M.C. (Eds.), 2023. Handbook of Mineralogy, Volume 1, Elements, Sulfides, Sulfosalts. Mineralogical Society of America, Chantilly, VA 20151-1110, USA. http://www.handbookofmineralogy.org. (Accessed 22 February 2023) (scheelite.pdf).

Armstrong, J.T., 1995. CITZAF: a package of correction programs for the quantitative electron microbeam X-ray analysis of thick polished materials, thin films, and particles. Microbeam Anal. 4, 177–200.

Bagnato, E., Tamburello, G., Granieri, D., Caliro, S., D'Agostino, F., Avino, R., Capecchiacci, F., Carandente, A., D'Alessandro, A., Minopoli, C., Santi, A., 2020. First simultaneous mercury and major volatiles characterization of atmospheric hydrothermal emissions at the Pisciarelli's fumarolic system (Campi Flegrei, Italy). J. Volcanol. Geotherm. Res. 406, 107074 https://doi.org/10.1016/j.jvolgeores.2020.107074.

Ballantyne, J.M., Moore, J.N., 1988. Arsenic geochemistry in geothermal systems. Geochim. Cosmochim. Acta 52, 475–483. https://doi.org/10.1016/0016-7037(88)90102-0.

Barbato, M., Cirillo, L., Menditto, L., Moretti, R., Nardini, S., 2018. Feasibility study of a geothermal energy system for indoor swimming pool in Campi Flegrei area. Thermal Science and Engineering Progress 6, 421–425. https://doi.org/10.1016/j.tsep.2018.02.013.

Barberi, F., Innocenti, F., Lirer, L., Munno, R., Pescatore, T., Santacroce, R., 1978. The Campanian Ignimbrite: a major prehistoric eruption in the Neapolitan area (Italy). Bull. Volcanol. 41, 10–31.

Barker, W.W., Parks, T.C., 1986. The thermodynamic properties of pyrrhotite and pyrite: a re-evaluation. Geochim. Cosmochim. Acta 50, 2185–2194. https://doi.org/10.1016/0016-7037(86)90073-6.

Barton Jr., P.B., 1991. Ore textures: problems and opportunities. Mineral. Mag. 55, 303–315. https://doi.org/10.1180/minmag.1991.055.380.02.

Barton Jr., P.B., Bethke, P.M., 1987. Chalcopyrite disease in sphalerite: pathology and epidemiology. Am. Mineral. 72, 451–467.

Belkin, H.E., De Vivo, B., 2004. Compositional variation of epidote in the Campi Flegrei geothermal field, Naples, Italy. In: 13th Annual V.M. Goldschmidt Conference, Copenhagen, Denmark, 5–11 June 2004, 68 (11S), p. A268.

Belkin, Harvey E., De Vivo, Benedetto, 2023. Compositional variation and zoning of epidote supergroup minerals in the Campi Flegrei geothermal field, Naples, Italy. Eur. J. Mineral. 35, 25–44. https://doi.org/10.5194/ejm-35-25-2023.

Belkin, H.E., Rolandi, G., Jackson, J.C., Cannatelli, C., Doherty, A.L., Petrosino, P., De Vivo, B., 2016. Mineralogy and geochemistry of the older (> 40 ka) ignimbrites on the Campanian Plain, southern Italy. J. Volcanol. Geotherm. Res. 323, 1–18. https://doi.org/10.1016/j.jvolgeores.2016.05.002.

Belkin, H.E., McAleer, R.J., De Vivo, B., Croke, M.R., 2023. Mofete and San Vito Geothermal Field Ore Mineralization Data: U.S. Geological Survey Data Release. https://doi.org/10.5066/P9HNDG4F.

Bodnar, R.J., Cannatelli, C., De Vivo, B., Lima, A., Belkin, H.E., Milia, A., 2007. Quantitative model for magma degassing and ground deformation (bradyseism) at Campi Flegrei, Italy: implications for future eruptions. Geology 35, 791–794. https://doi.org/10.1130/G23653A.1.

Bogie, I., Lawless, J., Morrison, K., 2000. Application of mineral deposit concepts to geothermal exploration. In: Iglesias, E. (Ed.), Proceedings of the World Geothermal Congress, International Geothermal Association Beppu-Morioka, Japan. Proceedings World Geothermal Congress 2000 Kyushu, Tohoku, Japan, pp. 1003–1006. ISBN 0473068117.

Browne, P.R.L., 1969. Sulfide mineralization in a Broadlands geothermal drill hole, Taupo volcanic zone, New Zealand. Econ. Geol. 64, 156–159. https://doi.org/10.2113/gsecongeo.64.2.156.

Browne, P.R.L., 1984. Occurrence of ore metals in some terrestrial geothermal systems. Abstract, Annual meeting of the American Institute of Mining, Metallurgical and Petroleum Engineers, Los Angeles, CA, USA, 26 Feb 1984.

Bruni, P., Chelini, W., Sbrana, A., Verdiani, G., 1985. Deep exploration of the S. Vito area (Pozzuoli-NA) Well S. Vito 1. In: International seminar on the Results of EC Geothermal Energy Research, vol. 3, pp. 390–406.

Bundschuh, J., Maity, J.P., 2015. Geothermal arsenic: occurrence, mobility and environmental implications. Renew. Sust. Energ. Rev. 100, 1214–1222. https://doi.org/10.1016/j.rser.2014.10.092.

Caprarelli, G., Tsutsumi, M., Turi, B., 1997. Chemical and isotopic signatures of the basement rocks from the Campi Flegrei geothermal field (Naples, southern Italy): inferences about the origin and evolution of its hydrothermal fluids. J. Volcanol. Geotherm. Res. 76, 63–82. https://doi.org/10.1016/S0377-0273(96)00072-8.

Carlino, S., Somma, R., Troise, C., De Natale, G., 2012. The geothermal exploration of Campanian volcanoes: historical review and future development. Renew. Sust. Energ. Rev. 16, 1004–1030. https://doi.org/10.1016/j.rser.2011.09.023.

Celico, P., Dall'Aglio, M., Ghiara, M.R., Stanzione, D., Brondi, M., Prosperi, M., 1992. Geochemical monitoring of the thermal fluids in the Phlegraean Fields from 1970 to 1990. Boll. Soc. Geol. Ital. 111, 409–422 (ISSN: 2038-1727).

Che, X.D., Linnen, R.L., Wang, R.C., Groat, L.A., Brand, A.A., 2013. Distribution of trace and rare earth elements in titanite from tungsten and molybdenum deposits in Yukon and British Columbia, Canada. Can. Mineral. 51, 415–438. https://doi.org/10.3749/canmin.51.3.415.

Chelini, W., Sbrana, A., 1987. Subsurface geology. In: Rosi, M., Sbrana, A. (Eds.), Phlegrean Fields, Consiglio Nazionale delle Ricerche, Quaderni De La Ricerca Scientifica 114, Roma, Italy, pp. 94–103 (ISSN 0556-9664.).

Chiodini, G., Caliro, S., Avino, R., Bagnato, E., Capecchiacci, F., Carandente, A., Cardellini, C., Minopoli, C., Tamburello, G., Tripaldi, S., Aiuppa, A., 2022. The hydrothermal system of the Campi Flegrei Caldera, Italy. In: Orsi, G., D'Antonio, M., Civetta, L. (Eds.), Campi Flegrei. Springer, Berlin, Heidelberg, pp. 239–255. https://doi.org/10.1007/978-3-642-37060-1_9.

Choi, S.G., Youm, S.J., 2000. Compositional variation of arsenopyrite and fluid evolution at the Ulsan deposit, southeastern Korea: a low-sulfidation porphyry system. Can. Mineral. 38, 567–583. https://doi.org/10.2113/gscanmin.38.3.567.

Daliran, F., 2008. The carbonate rock-hosted epithermal gold deposit of Agdarreh, Takab geothermal field, NW Iran—hydrothermal alteration and mineralisation. Mineral. Deposita 43, 383–404. https://doi.org/10.1007/s00126-007-0167-x.

De Vivo, B., Lima, A., 2006. A hydrothermal model for ground movements (bradyseism) at Campi Flegrei, Italy. In: De Vivo, B. (Ed.), Volcanism in the Campania Plain - Vesuvius, Campi Flegrei and Ignimbrites. Elsevier, Amsterdam, Netherlands, pp. 289–317. https://doi.org/10.1016/S1871-644X(06)80028-8.

De Vivo, B., Belkin, H.E., Barbieri, M., Chelini, W., Lattanzi, P., Lima, A., Tolomeo, L., 1989. The Campi Flegrei (Italy) geothermal system: a fluid inclusion study of the Mofete and San Vito fields. J. Volcanol. Geotherm. Res. 36, 303–326. https://doi.org/10.1016/0377-0273(89)90076-0.

De Vivo, B., Rolandi, G., Gans, P.B., Calvert, A., Bohrson, W.A., Spera, F.J., Belkin, H.E., 2001. New constraints on the pyroclastic eruptive history of the Campanian volcanic Plain, (Italy). Mineral. Petrol. 73, 47–65. https://doi.org/10.1007/s007100170010.

De Vivo, B., Lima, A., Albanese, S., and Cicchella, D., 2011. Naturally occurring arsenic and radioactivity in the Neapolitan Volcanic Province as a source of a potential hazard for human health. In: Proceedings of GEOMED 2011, 4th International Conference on Medical Geology, Bari, Italy, 35.

Desborough, G.A., Czamanske, G.K., 1973. Sulfides in eclogite nodules from a kimberlite pipe, South Africa, with comments on violarite stoichiometry. Am. Mineral. 58, 195–202.

Di Vito, M., Lirer, L., Mastrolorenzo, G., Rolandi, G., 1987. The 1538 Monte Nuovo eruption (Campi Flegrei, Italy). Bull. Volcanol. 49, 608–615. https://doi.org/10.1007/BF01079966.

Einaudi, M.T., Hedenquist, J.W., Inan, E.E., Einaudi, M.T., Hedenquist, J.W., Inan, E.E., 2003. Sulfidation state of hydrothermal fluids: the porphyry-epithermal transition and beyond. In: Simmons, S.F., Graham, I. (Eds.), Society of Economic Geologists Special Publication 10, pp. 285–313. https://doi.org/10.5382/sp.10.15.

Fedele, A., Pedone, M., Moretti, R., Wiersberg, T., Somma, R., Troise, C., De Natale, G., 2017. Real-time quadrupole mass spectrometry of hydrothermal gases from the unstable Pisciarelli fumaroles (Campi Flegrei): trends, challenges, and processes. Int. J. Mass Spectrom. 415, 44–54. https://doi.org/10.1016/j.ijms.2017.02.006.

Fischer, M., Röller, K., Küster, M., Stöckhert, B., McConnell, V.S., 2003. Open fissure mineralization at 2600 m depth in Long Valley Exploratory Well (California)–insight into the history of the hydrothermal system. J. Volcanol. Geotherm. Res. 127, 347–363. https://doi.org/10.1016/S0377-0273(03)00176-8.

Fontboté, L., Kouzmanov, K., Chiaradia, M., Pokrovski, G.S., 2017. Sulfide minerals in hydrothermal deposits. Elements 13, 97–103. https://doi.org/10.2113/gselements.13.2.97.

Gaeta, F.S., De Natale, G., Peluso, F., Mastrolorenzo, G., Castagnolo, D., Troise, C., Pingue, F., Mita, D.G., Rossano, S., 1998. Genesis and evolution of unrest episodes at Campi Flegrei caldera: the role of thermal fluid-dynamical processes in the geothermal system. J. Geophys. Res. Solid Earth 103 (B9), 20921–20933. https://doi.org/10.1029/97JB03294.

Giacomelli, L., Scandone, R., 2012. History of the exploitation of thermo-mineral resources in Campi Flegrei and Ischia, Italy. J. Volcanol. Geotherm. Res. 209, 19–32. https://doi.org/10.1016/j.jvolgeores.2011.10.004.

Goff, F., Gardner, J.N., 1994. Evolution of a mineralized geothermal system, Valles Caldera, New Mexico. Econ. Geol. 89, 1803–1832. https://doi.org/10.2113/gsecongeo.89.8.1803.

Grancea, L., Bailly, L., Leroy, J., Banks, D., Marcoux, E., Milési, J., Cuney, M., André, A., Istvan, D., Fabre, C., 2002. Fluid evolution in the Baia Mare epithermal gold/polymetallic district, Inner Carpathians, Romania. Mineral. Deposita 37, 630–647. https://doi.org/10.1007/s00126-002-0276-5.

Grant, H.L., Hannington, M.D., Hardardóttir, V., Fuchs, S.H., Schumann, D., 2020. Trace metal distributions in sulfide scales of the seawater-dominated Reykjanes geothermal system: constraints on sub-seafloor hydrothermal mineralizing processes and metal fluxes. Ore Geol. Rev. 116, 103145 https://doi.org/10.1016/j.oregeorev.2019.103145.

Guglielminetti, M., 1986. Mofete geothermal field. Geothermics 15, 781–790. https://doi.org/10.1016/0375-6505(86)90091-X.

Guo, Q., Li, Y., Luo, L., 2019. Tungsten from typical magmatic hydrothermal systems in China and its environmental transport. Sci. Total Environ. 657, 1523–1534. https://doi.org/10.1016/j.scitotenv.2018.12.146.

Hanano, M., 2004. Contribution of fractures to formation and production of geothermal resources. Renew. Sust. Energ. Rev. 8, 223–236. https://doi.org/10.1016/j.rser.2003.10.007.

Hardardóttir, V., Ármannsson, H., Þórhallsson, S., 2005. Characterization of sulfide-rich scales in brine at Reykjanes. In: Proceedings World Geothermal Congress 2005 Antalya, Turkey, 24–29 April 2005, ISBN 9759833204.

Harijoko, A., Hapsari, K., Wibowo, Y.T., Atmaja, R.W., Nurpratama, M.I., 2015. The sulfide minerals deposit in the geothermal pipes of Dieng Geothermal Field, Indonesia. In: Roland, N., Boyd, T. (Eds.), Proceedings World Geothermal Congress 2015, pp. 1–5. Melbourne, Australia.

Hazen, R.M., Finger, L.W., Mariathasan, J.W.E., 1985. High-pressure crystal chemistry of scheelite-type tungstates and molybdates. J. Phys. Chem. Solids 46, 253–263. https://doi.org/10.1016/0022-3697(85)90039-3.

Hedenquist, J.W., Lowenstern, J.B., 1994. The role of magmas in the formation of hydrothermal ore deposits. Nature 370 (6490), 519–527. https://doi.org/10.1038/370519a0.

Huebner, J.S., Woodruff, M.E., 1985. Chemical compositions and critical evaluation of microprobe standards available from the Reston microprobe facility. In: U.S. Geological Survey Open File Report 85-718. https://doi.org/10.3133/ofr85718 (45 pp.).

Hulen, J.B., Nielson, D.L., 1987. Hydraulic fracturing and hydrothermal brecciation in active geothermal systems. In: Geothermal Resources Council, Transactions, 11, pp. 473–478. ISSN 01935933.

Hulen, J.B., Nielson, D.L., Goff, F., Gardner, J.N., Charles, R.W., 1987. Molybdenum mineralization in an active geothermal system, Valles caldera, New Mexico. Geology 15, 748–752. https://doi.org/10.1130/0091-7613(1987)15<748:MMIAAG>2.0.CO;2.

Iorio, M., Punzo, M., Carotenuto, A., Cavuoto, G., Corniello, A., Di Fiore, V., Donnarumma, G., Fedi, M., Massarotti, N., Pelosi, N., Tarallo, D., 2024. Shallow geothermal field multidisciplinary exploration: new data from Campi Flegrei caldera (CFc) for low—middle enthalpy resource exploitation. Geothermics 121, 103049. https://doi.org/10.1016/j.geothermics.2024.103049.

Isaia, R., Di Giuseppe, M.G., Natale, J., Tramparulo, F.D.A., Troiano, A., Vitale, S., 2021. Volcano-tectonic setting of the Pisciarelli fumarole field, Campi Flegrei caldera, southern Italy: insights into fluid circulation patterns and hazard scenarios. Tectonics 40 (5), e2020TC006227. https://doi.org/10.1029/2020TC006227.

Kakimoto, P.K., Browne, P.R.L., 1986. Mass transfer during hydrothermal alteration at the Tauhara Geothermal Field. In: Proceeding of the 8th New Zealand Geothermal Workshop, Auckland, NZ, ISBN 0-86869-075-9, pp. 10–111.

Kerestedjian, T., 1997. Chemical and morphological features of arsenopyrite, concerning its use as a geothermometer. Mineral. Petrol. 60, 231–243. https://doi.org/10.1007/BF01173710.

Kretschmar, U., Scott, S.D., 1976. Phase relations involving arsenopyrite in the system Fe-As-S and their application. Can. Mineral. 14, 364–386 (ISSN: 1499-1276).

Krupp, R.E., Seward, T.M., 1987. The Rotokawa geothermal system, New Zealand; an active epithermal gold-depositing environment. Econ. Geol. 82, 1109–1129. https://doi.org/10.2113/gsecongeo.82.5.1109.

Lima, A., De Vivo, B., Spera, F.J., Bodnar, R.J., Milia, A., Nunziata, C., Belkin, H.E., Cannatelli, C., 2009. Thermodynamic model for uplift and deflation episodes (bradyseism) associated with magmatic–hydrothermal activity at the Campi Flegrei (Italy). Earth Sci. Rev. 97 (1–4), 44–58. https://doi.org/10.1016/j.earscirev.2009.10.001.

Lima, A., Bodnar, R.J., De Vivo, B., Spera, F.J., Belkin, H.E., 2021. Interpretation of recent unrest events (bradyseism) at Campi Flegrei, Napoli (Italy): comparison of models based on cyclical hydrothermal events versus shallow magmatic intrusive events. Geofluids 2021, 1–16. https://doi.org/10.1155/2021/2000255, 2021.

Mahon, W.A.J., McDowell, G.D., 1977. Magmatic-volcanic steam: its role in geothermal area. In: Ellis, A.J. (Ed.), Geochemistry, DSIR Bulletin, vol. 218, pp. 11–17.

Marini, L., Principe, C., Lelli, M., 2022. The Solfatara Magmatic-Hydrothermal System. Springer, Cham, Switzerland. ISBN 9783030984700.

McKibben, M.A., Elders, W.A., 1985. Fe-Zn-Cu-Pb mineralization in the Salton Sea geothermal system, Imperial Valley, California. Econ. Geol. 80, 539–559. https://doi.org/10.2113/gsecongeo.80.3.539.

McKibben, M.A., Andes Jr., J.P., Williams, A.E., 1988. Active ore formation at a brine interface in metamorphosed deltaic lacustrine sediments; the Salton Sea geothermal system, California. Econ. Geol. 83, 511–523. https://doi.org/10.2113/gsecongeo.83.3.511.

Milési, J.P., Marcoux, E., Nehlig, P., Sunarya, Y., Sukandar, A., Felenc, J., 1994. Cirotan, West Java, Indonesia; a 1.7 Ma hybrid epithermal Au-Ag-Sn-W deposit. Econ. Geol. 89, 227–245. https://doi.org/10.2113/gsecongeo.89.2.227.

Misra, K.C., Fleet, M.E., 1974. Chemical composition and stability of violarite. Econ. Geol. 69, 391–403. https://doi.org/10.2113/gsecongeo.69.3.391.

Morimoto, N., Clark, L.A., 1961. Arsenopyrite crystal-chemical relations. Am. Mineral. 46, 1448–1469.

Mormone, A., Tramelli, A., Di Vito, M.A., Piochi, M., Troise, C., De Natale, G., 2011. Secondary hydrothermal minerals in buried rocks at the Campi Flegrei caldera, Italy: a possible tool to understand the rock-physics and to assess the state of the volcanic system. Periodico di Mineralogia 80 (3 (Spec. Issue)), 385–406. https://doi.org/10.2451/2011PM0027.

Pals, D.W., Spry, P.G., 2003. Telluride mineralogy of the low-sulfidation epithermal Emperor gold deposit, Vatukoula, Fiji. Mineral. Petrol. 79, 285–307. https://doi.org/10.1007/s00710-003-0013-5.

Piochi, M., Mastrolorenzo, G., Pappalardo, L., 2005. Magma ascent and eruptive processes from textural and compositional features of Monte Nuovo pyroclastic products, Campi Flegrei, Italy. Bull. Volcanol. 67, 663–678. https://doi.org/10.1007/s00445-005-0410-1.

Piochi, M., Kilburn, C.R.J., Di Vito, M.A., Mormone, A., Tramelli, A., Troise, C., De Natale, G., 2014. The volcanic and geothermally active Campi Flegrei caldera: an integrated multidisciplinary image of its buried structure. Int. J. Earth Sci. 103, 401–421. https://doi.org/10.1007/s00531-013-0972-7.

Piochi, M., Cantucci, B., Montegrossi, G., Currenti, G., 2021. Hydrothermal alteration at the San Vito area of the Campi Flegrei geothermal system in Italy: mineral review and geochemical modeling. Minerals 11, 810. https://doi.org/10.3390/min11080810.

Pokrovski, G.S., Kara, S., Roux, J., 2002. Stability and solubility of arsenopyrite, FeAsS, in crustal fluids. Geochim. Cosmochim. Acta 66, 2361–2378. https://doi.org/10.1016/S0016-7037(02)00836-0.

Poulin, R.S., McDonald, A.M., Kontak, D.J., McClenaghan, M.B., 2016. On the relationship between cathodoluminescence and the chemical composition of scheelite from geologically diverse ore-deposit environments. Can. Mineral. 54, 147–1173. https://doi.org/10.3749/canmin.1500023.

Raymond, J., Williams-Jones, A.E., Clark, J.R., 2005. Mineralization associated with scale and altered rock and pipe fragments from the Berlin geothermal field, El Salvador; implications for metal transport in natural systems. J. Volcanol. Geotherm. Res. 145, 81–96. https://doi.org/10.1016/j.jvolgeores.2005.01.003.

Reich, M., Román, N., Barra, F., Morata, D., 2020. Silver-rich chalcopyrite from the active Cerro Pabellón geothermal system. Northern Chile. Minerals 10, 113. https://doi.org/10.3390/min10020113.

Reyes, A.G., Trompetter, W.J., Britten, K., Searle, J., 2002. Mineral deposits in the Rotokawa geothermal pipelines, New Zealand. J. Volcanol. Geotherm. Res. 119, 215–223. https://doi.org/10.1016/S0377-0273(02)00355-4.

Roedder, E., 1984. Fluid inclusions. In: Reviews in Mineralogy, vol. 12. Mineralogical Society of America, Chantilly, VA, ISBN 0-939950-16-2.

Rolandi, G., Bellucci, F., Heisler, M.T., Belkin, H.E., De Vivo, B., 2003. Tectonic controls on the genesis of ignimbrites from the Campanian Volcanic Zone, Southern Italy. Mineral. Petrol. 79, 3–31. https://doi.org/10.1007/s00710-003-0014-4.

Rolandi, G., Di Lascio, M., Rolandi, R., 2020a. The Neapolitan Yellow Tuff eruption as the source of the Campi Flegrei caldera. In: De Vivo, B., Belkin, H.E., Rolandi, G. (Eds.), Vesuvius, Campi Flegrei, and Campanian Volcanism. Elsevier, Amsterdam, Netherlands, pp. 273–296. https://doi.org/10.1016/B978-0-12-816454-9.00011-0.

Rolandi, G., De Natale, G., Kilburn, C.R., Troise, C., Somma, R., Di Lascio, M., Fedele, A., Rolandi, R., 2020b. The 39 ka Campanian Ignimbrite eruption: new data on source area in the Campanian Plain. In: De Vivo, B., Belkin, H.E., Rolandi, G. (Eds.), Vesuvius, Campi Flegrei, and Campanian Volcanism. Elsevier, Amsterdam, Netherlands, pp. 175–205. https://doi.org/10.1016/B978-0-12-816454-9.00008-0.

Phlegrean fields. In: Rosi, M., Sbrana, A. (Eds.), 1987. Consiglio Nazionale delle Ricerche, Quaderni De La Ricerca Scientifica 114, Roma, Italy, pp. 94–103 (ISSN 0556-9664).

Rosi, M., Sbrana, A., Principe, C., 1983. The Phlegrean Fields: structural evolution, volcanic history and eruptive mechanisms. J. Volcanol. Geotherm. Res. 17, 273–288. https://doi.org/10.1016/0377-0273(83)90072-0.

Sadovnikov, S.I., Gusev, A.I., 2019. Argentite-Acanthite transformation in silver sulfide as a disorder-order transition. J. Exp. Theor. Phys. Lett. 109, 584–588. https://doi.org/10.1134/S0021364019090145.

Sander, M.V., Mitchell, P.A., 1988. Close resemblance between the active geothermal system at Wairakei. New Zealand, and the Tertiary epithermal Au-Ag deposit at Round Mountain, Nevada, USA-except for amount, position, and timing of Au mineralisation (extended abs.). In: Goode, A.D.T., Bosma, L.I. (Eds.), Bicentennial Gold 88, Extended Abstracts, Oral Programme, Geological Society of Australia, Abs. Series, vol. 22, ISBN 0909869626, pp. 290–295.

Schenk, P., Höll, R., 1991. Evolution of fluids and metamorphic ore remobilization in the Felbertal scheelite deposit, Eastern Alps. Ore Geol. Rev. 6, 425–434. https://doi.org/10.1016/0169-1368(91)90039-A.

Simmons, S.F., Kirby, S., 2020. Western USA assessment of high value materials in geothermal and produced fluids. In: Proceedings World Geothermal Congress 2020+1, Reykjavik, Iceland, April–October 2021, pp. 1–11. http://www.geothermal-energy.org/pdf/IGAstandard/WGC/2020/39001.pdf.

Skinner, B.J., White, D.E., Rose, H.J., Mays, R.E., 1967. Sulfides associated with the Salton Sea geothermal brine. Econ. Geol. 62, 316–330. https://doi.org/10.2113/gsecongeo.62.3.316.

Tenailleau, C., Pring, A., Etschmann, B., Brugger, J., Grguric, B., Putnis, A., 2006. Transformation of pentlandite to violarite under mild hydrothermal conditions. Am. Mineral. 91, 706–709. https://doi.org/10.2138/am.2006.2131.

Troise, C., De Natale, G., Schiavone, R., Somma, R., Moretti, R., 2019. The Campi Flegrei caldera unrest: discriminating magma intrusions from hydrothermal effects and implications for possible evolution. Earth Sci. Rev. 188, 108–122.

Valentino, G.M., Stanzione, D., 2003. Source processes of the thermal waters from the Phlegraean Fields (Naples, Italy) by means of the study of selected minor and trace elements distribution. Chem. Geol. 194, 245–274. https://doi.org/10.1016/S0009-2541(02)00196-1.

Vaughan, D.J., Craig, J.R., 1985. The crystal chemistry of iron-nickel thiospinels. Am. Mineral. 70, 1036–1043.

Wang, C., Winterfeld, P., Johnston, B., Wu, Y.S., 2020. An embedded 3D fracture modeling approach for simulating fracture-dominated fluid flow and heat transfer in geothermal reservoirs. Geothermics 86, 101831. https://doi.org/10.1016/j.geothermics.2020.101831.

Wang, X.S., Williams-Jones, A.E., Hu, R.Z., Shang, L.B., Bi, X.W., 2021. The role of fluorine in granite-related hydrothermal tungsten ore genesis: results of experiments and modeling. Geochim. Cosmochim. Acta 292, 170–187. https://doi.org/10.1016/j.gca.2020.09.032.

Wang, X.S., Williams-Jones, A.E., Hu, R.Z., Jiang, Z.Q., Shang, L.B., Bi, X.W., 2023. Apatite and fluorite control the transport of tungsten in calcium-bearing hydrothermal fluids. Geochim. Cosmochim. Acta 346, 1–14. https://doi.org/10.1016/j.gca.2023.02.001.

Ward, K.T., Brown, K.L., Webster-Brown, J., 2006. Mineral Precipitation in the Rotokawa Geothermal Power Station, New Zealand. In: Proceedings 28th New Zealand Geothermal Workshop, Auckland, New Zealand (6 pp., ISSN 1177-7745).

Watanabe, K., Takahashi, H., 1995. Fractal geometry characterization of geothermal reservoir fracture networks. J. Geophys. Res. Solid Earth 100 (B1), 521–528. https://doi.org/10.1029/94JB02167.

White, D.E., 1981. Active geothermal systems and hydrothermal ore deposits. In: Skinner, B.J. (Ed.), Economic Geology 75th Anniversary Volume, pp. 392–423. https://doi.org/10.5382/AV75.12.

Zamora, M., Sartoris, G., Chelini, W., 1994. Laboratory measurements of ultrasonic wave velocities in rocks from the Campi Flegrei volcanic system and their relation to other field data. J. Geophys. Res. 99, 13553–13561. https://doi.org/10.1029/94JB00121.

Zhao, Q., Guo, Q., Luo, L., Yan, K., 2021. Tungsten accumulation in hot spring sediments resulting from preferred sorption of aqueous polytungstates to goethite. Int. J. Environ. Res. Public Health 18, 12629. https://doi.org/10.3390/ijerph182312629.